

## Aerosol optical properties measured on board the *Ronald H. Brown* during ACE-Asia as a function of aerosol chemical composition and source region

P. K. Quinn,<sup>1,2</sup> D. J. Coffman,<sup>1,2</sup> T. S. Bates,<sup>1,2</sup> E. J. Welton,<sup>3</sup> D. S. Covert,<sup>4</sup> T. L. Miller,<sup>1,2</sup> J. E. Johnson,<sup>1,2</sup> S. Maria,<sup>5</sup> L. Russell,<sup>5</sup> R. Arimoto,<sup>6</sup> C. M. Carrico,<sup>7,8</sup> M. J. Rood,<sup>9</sup> and J. Anderson<sup>10</sup>

Received 25 July 2003; revised 17 November 2003; accepted 2 February 2004; published 17 September 2004.

[1] During the Asian Pacific Regional Aerosol Characterization Experiment (ACE-Asia) intensive field campaign conducted in the spring of 2001, aerosol properties were measured on board the R/V *Ronald H. Brown* to study the effects of the Asian aerosol on atmospheric chemistry and climate in downwind regions. Aerosol properties measured in the marine boundary layer included chemical composition; number size distribution; and light scattering, hemispheric backscattering, and absorption coefficients. In addition, optical depth and vertical profiles of aerosol 180° backscatter were measured. Aerosol within the ACE-Asia study region was found to be a complex mixture resulting from marine, pollution, volcanic, and dust sources. Presented here as a function of air mass source region are the mass fractions of the dominant aerosol chemical components, the fraction of the scattering measured at the surface due to each component, mass scattering efficiencies of the individual components, aerosol scattering and absorption coefficients, single scattering albedo, Ångström exponents, optical depth, and vertical profiles of aerosol extinction. All results, except aerosol optical depth and the vertical profiles of aerosol extinction, are reported at a relative humidity of  $55 \pm 5\%$ . An overdetermined data set was collected so that measured and calculated aerosol properties could be compared, internal consistency in the data set could be assessed, and sources of uncertainty could be identified. By adjusting the measured size distribution to take into account nonsphericity of the dust aerosol, calculated and measured aerosol mass and scattering coefficients agreed within overall experimental uncertainties. Differences between measured and calculated aerosol absorption coefficients were not within reasonable uncertainty limits, however, and may indicate the inability of Mie theory and the assumption of internally mixed homogeneous spheres to predict absorption by the ACE-Asia aerosol. Mass scattering efficiencies of non-sea-salt sulfate aerosol, sea salt, submicron particulate organic matter, and dust found for the ACE-Asia aerosol are comparable to values estimated for ACE 1, Aerosols99, and the Indian Ocean Experiment (INDOEX). Unique to the ACE-Asia aerosol were the large mass fractions of dust, the dominance of dust in controlling the aerosol optical properties, and the interaction of dust with soot aerosol. **INDEX TERMS:** 0305 Atmospheric Composition and Structure: Aerosols and particles (0345, 4801); 0345 Atmospheric Composition and Structure: Pollution—urban and regional (0305); 0365 Atmospheric Composition and Structure: Troposphere—composition and chemistry; **KEYWORDS:** aerosol optical properties, aerosol chemical composition, ACE-Asia

**Citation:** Quinn, P. K., et al. (2004), Aerosol optical properties measured on board the *Ronald H. Brown* during ACE-Asia as a function of aerosol chemical composition and source region, *J. Geophys. Res.*, 109, D19S01, doi:10.1029/2003JD004010.

<sup>1</sup>Pacific Marine Environmental Laboratory, National Oceanic and Atmospheric Administration, Seattle, Washington, USA.

<sup>2</sup>Also at Joint Institute for the Study of the Atmosphere and Ocean, University of Washington, Seattle, Washington, USA.

<sup>3</sup>Goddard Space Flight Center, NASA, Greenbelt, Maryland, USA.

<sup>4</sup>Joint Institute for the Study of the Atmosphere and Ocean, University of Washington, Seattle, Washington, USA.

<sup>5</sup>Department of Chemical Engineering, Princeton University, Princeton, New Jersey, USA.

<sup>6</sup>Carlsbad Environmental Monitoring and Research Center, New Mexico State University, Carlsbad, New Mexico, USA.

<sup>7</sup>Department of Atmospheric Science, Colorado State University, Fort Collins, Colorado, USA.

<sup>8</sup>Also at Department of Civil and Environmental Engineering, University of Illinois, Urbana, Illinois, USA.

<sup>9</sup>Department of Civil and Environmental Engineering, University of Illinois, Urbana, Illinois, USA.

<sup>10</sup>Department of Mechanical and Aerospace Engineering, Arizona State University, Tempe, Arizona, USA.

## 1. Introduction

[2] The third Aerosol Characterization Experiment (ACE) focused on Asia (ACE-Asia) to study the effects of the aerosol emanating from this region on atmospheric chemistry and climate. The experiment was conducted during the spring (mid-March to mid-April of 2001) to capture outbreaks of Asian dust associated with frontal systems moving eastward through the dust-producing regions. The dust is routinely transported to Korea and Japan, out over the North Pacific, and occasionally as far east as North America [Prospero *et al.*, 2002]. *En route* over China and coastal regions, the dust aerosol mixes with aerosol derived from industrial, combustion, volcanic, and natural sources. Hence by the time the Asian aerosol has reached the western margin of the Pacific Ocean it is a complex mixture of dust, organics, elemental carbon, sulfates, nitrate, sea salt, and liquid water.

[3] ACE-Asia was a multiplatform international experiment [Huebert *et al.*, 2003] with coordinated measurements at several ground sites and on board three aircraft and two ships. The results presented here are from measurements made on board the NOAA R/V *Ronald H. Brown* (RHB). RHB left Honolulu, Hawaii on 15 March (day of year (DOY) 74) and headed to the ACE-Asia study region. During the transit across the Pacific, marine air with little influence from continental sources was sampled. Eleven days later on 26 March (DOY 85) and 2000 km from the east coast of Japan, RHB encountered continentally influenced air. For the rest of the cruise, air masses heavily impacted by Asian emissions were sampled.

[4] The measurements on board RHB in context with the prevailing meteorology allowed for the determination of the aerosol chemical composition, physical properties, and optical properties for a variety of aerosol source regions. Aerosol optical properties are presented as a function of aerosol chemical composition and source region. In addition, columnar information is presented in the form of aerosol optical depth, vertical distributions of aerosol extinction, and the fraction of light scattering due to aerosol in the boundary layer. This analysis is analogous to those previously reported for ACE 1 (remote Southern Ocean) [Quinn *et al.*, 1998], Aerosols99 (a cruise across the Atlantic) [Quinn *et al.*, 2001], and INDOEX (The Indian Ocean Experiment) [Quinn *et al.*, 2002] and, thus, adds to a growing body of regional aerosol characterizations.

[5] To determine the effect of the prevailing meteorology and aerosol sources on aerosol chemical and optical properties, sampling times were separated into seven categories based on geographical source regions indicated by the air mass back trajectories. These regions, which identify the dominant source of the aerosol, are labeled as (1) Marine – 4 North Pacific, (2) Polluted – Korea/Japan, (3) Polluted – Japan, (4) Volcano + Polluted, (5) Dust – Frontal, (6) Dust + Korea, and (7) Dust + Shanghai. Figure 1 shows the cruise track and trajectories typical of each region. Throughout the paper, region refers to the source region of the sampled aerosol and not the geographical region where the measurements were made.

[6] As pointed out by Anderson *et al.* [2003], the degree of variability presented here is limited by the sampling strategy and meteorological conditions that were encoun-

tered during the experiment. Most likely, RHB did not sample the full range or combination of source regions that impact Asian aerosol during the spring. In addition, each source region and resulting aerosol mixture most likely was not sampled in proportion to its true prevalence (as is indicated by the varying number of samples collected for each source region). However, these results are a starting point for assessing the impacts of Asian aerosol on regional atmospheric chemistry and climate and should be extended further by additional measurements and atmospheric models.

[7] The aerosol encountered in the ACE-Asia region was a complex mixture of marine, volcanic, pollution, and dust chemical components. Electron microscope images reveal a wide range of mixing states such that individual black carbon cenospheres, dust-soot aggregates, and silicate fly ash were present in the same sample. The presence of large quantities of dust introduced the complexity of nonspherical particle shapes. All of these issues combined to make the ACE-Asia aerosol particularly challenging to measure and model accurately. Our approach for understanding the impact of these complexities on the measurements and model was to produce an overdetermined data set. Such a data set allows for closure tests to be performed between measured and calculated parameters, to test for internal consistency in the data set, and to identify sources of uncertainty in the measurement and model methods.

[8] We start the paper with a discussion of the mass, scattering, and absorption closure results and what they reveal about the ACE-Asia aerosol. We then focus on the measurements made 18 m above sea level (asl) and describe the mass fractions of the chemical components observed for each source region as well as the regional size distributions and optical properties. To conclude the description of the surface measurements, we discuss the contribution made by the dominant chemical components to the light scattering in each region. The last part of the results section focuses on the optical measurements made in the atmospheric column above the ship. Finally, in the conclusions we summarize our major findings and suggest improvements in aerosol measurement and modeling methods that should further our understanding of complex aerosol mixtures such as those found downwind of Asia.

## 2. Measurements

### 2.1. Aerosol Sample Inlet

[9] Sample air for the chemical, physical, and optical measurements was drawn through a 6 m sample mast. The entrance to the mast was 18 m above sea level and forward of the ship's stack. The transmission efficiency of the inlet for particles with aerodynamic diameters less than 6.5  $\mu\text{m}$  (the largest size tested) is greater than 95% [Bates *et al.*, 2002]. Air was sampled only when the concentration of particles greater than 15 nm in diameter indicated the sample air was free of local contamination (i.e., there were no rapid increases in particle concentration), the relative wind speed was greater than 3  $\text{m s}^{-1}$ , and the relative wind was forward of the beam.

[10] The last 1.5 m of the mast were heated to establish a stable reference relative humidity (RH) for the sample air of

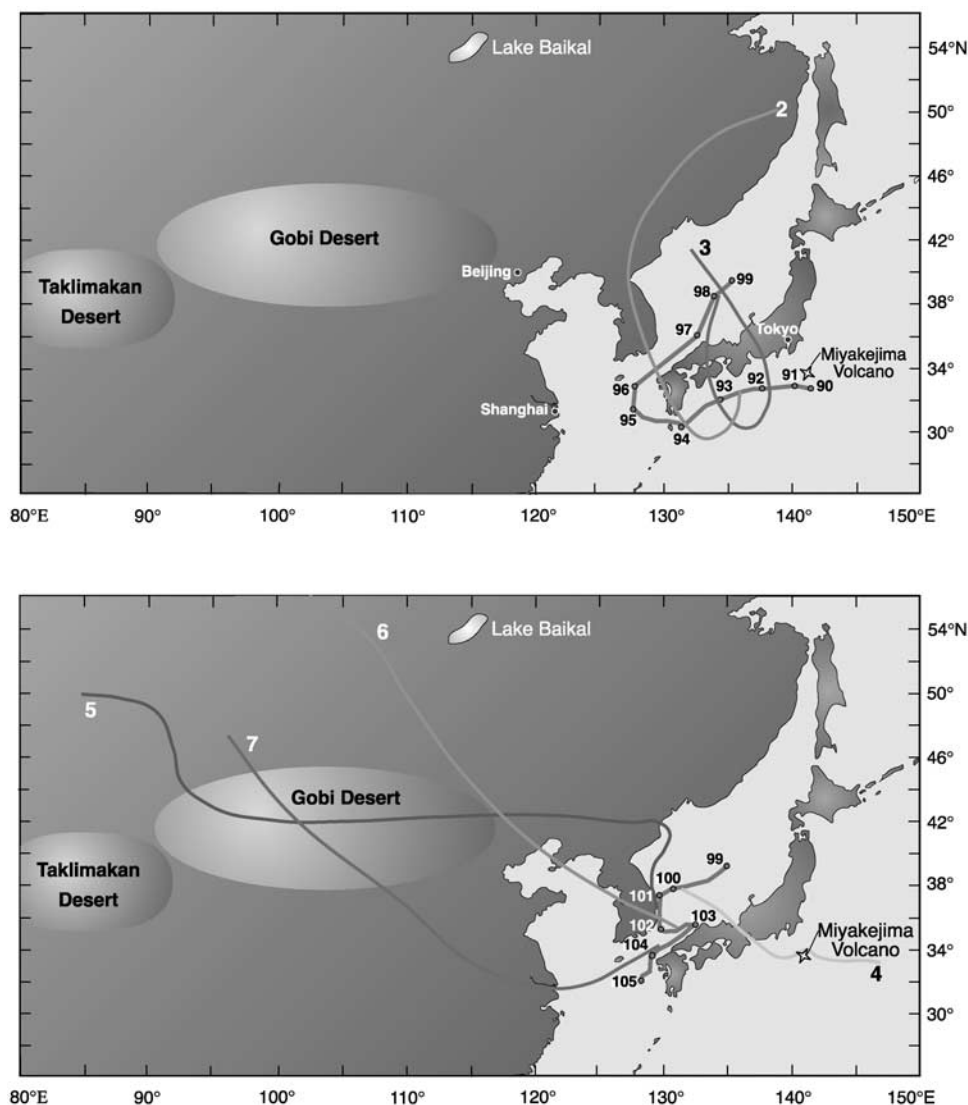


**Figure 1.** Cruise track of the NOAA R/V *Ronald H. Brown* (shown as a solid line numbered with DOY) during the Asian Pacific Regional Aerosol Characterization Experiment (ACE-Asia) for (top) DOY 90–99 and (bottom) DOY 99–105. Not shown is the transit from Hawaii to Japan, which occurred from DOY 74 to 90 primarily between 31° and 34.5°N. Also shown are 5 day air mass back trajectories with an arrival height of 500 m for regions 2–7, where 2 is Polluted – Korea/Japan, 3 is Polluted – Japan, 4 is Volcano + Polluted, 5 is Dust – Frontal Passage, 6 is Dust + Korea, and 7 is Dust + Shanghai. Each day back in time is indicated. The trajectory for region 5 (Dust – Frontal Passage) indicates the flow at 2500 m; the 500 m flow was from China, Korea, and the Sea of Japan. See color version of this figure in the HTML.

$55 \pm 5\%$ . A stable reference RH allows for constant instrumental size segregation in spite of variations in ambient RH and results in chemical, physical, and optical measurements which are directly comparable. In addition, measurement at a constant reference RH makes it possible, with the knowledge of appropriate growth factors, for end users of the data set (process, chemical transport, and radiative transfer models) to adjust the measured parameters to a desired RH. A reference RH of 55% was chosen because it is above the crystallization humidity of most aerosol components and component mixtures [Carrico *et al.*, 2003; Shaw and Rood, 1990]. For the atmospheric conditions encountered during ACE-Asia, it was possible to maintain 55% RH without excessive heating of the aerosol. On average, the aerosol was

heated 5.1°C above the ambient temperature. All results of the in situ measurements are reported at  $55 \pm 5\%$  RH. Further details about the sample inlet can be found in the work of Bates *et al.* [2004].

## 2.2. Aerosol Mass and Chemical Composition

### 2.2.1. Sample Collection for Chemical Analysis

[11] Two-stage multijet cascade impactors [Bernier *et al.*, 1979] sampling air at  $55 \pm 5\%$  RH were used to determine sub- and supermicron concentrations of aerosol mass, inorganic ions, organic and elemental carbon (OC and EC), and inorganic oxidized material (IOM). These data were used to calculate relative contributions of the chemical components to the aerosol mass as a function of source region.

[12] Aerosol mass and IOM were determined from the same impactor. Additional impactors were used for the inorganic ion and the OC/EC analyses. The 50% aerodynamic cutoff diameters of the impactors,  $D_{50,aero}$ , were 1.1 and 10  $\mu\text{m}$ . The RH of the sampled air stream was measured a few cm upstream from the impactors. Throughout the paper submicron refers to particles with  $D_{aero} < 1.1 \mu\text{m}$  at 55% RH and supermicron refers to particles with  $1.1 \mu\text{m} < D_{aero} < 10 \mu\text{m}$  at 55% RH. Sub-10  $\mu\text{m}$  refers to particles with  $D_{aero} < 10 \mu\text{m}$  at 55% RH.

[13] A 12  $\mu\text{m}$  impaction stage at the inlet of each impactor was coated with silicone grease to prevent the bounce of larger particles onto the downstream stages. A Tedlar film placed on the impactor jet plate having a  $D_{50,aero}$  of 10  $\mu\text{m}$  was sprayed with silicone lubricant for the same reason. Since films placed on downstream jet plates were used for chemical analysis, they were not sprayed to avoid contamination. All handling of the substrates was done in an  $\text{NH}_3$ - and  $\text{SO}_2$ - free glove box. Blank levels were determined by loading an impactor with substrates but not drawing any air through it. Sampling periods ranged from 2.5 to 7 hours during the day and 4 to 12 hours at night.

[14] In addition, seven-stage multijet cascade impactors ( $D_{50,aero}$  of 0.18, 0.31, 0.55, 1.1, 2.0, 4.1, and 10  $\mu\text{m}$ ) were used to obtain size distributions of aerosol mass, inorganic ions, OC, EC, and IOM for use in the calculation of aerosol density, refractive index, scattering, and absorption. These samples were treated in the same manner as the two-stage impactor samples. Sampling periods ranged from 7 to 12 hours.

### 2.2.2. Inorganic Ions

[15] Sub- and supermicron concentrations of  $\text{Cl}^-$ ,  $\text{NO}_3^-$ ,  $\text{SO}_4^{2-}$ , methanesulfonate ( $\text{MSA}^-$ ),  $\text{Na}^+$ ,  $\text{NH}_4^+$ ,  $\text{K}^+$ ,  $\text{Mg}^{+2}$ , and  $\text{Ca}^{+2}$  were determined by ion chromatography (IC) [Quinn *et al.*, 1998]. Substrate materials and handling information can be found in the work of Quinn *et al.* [2002].

[16] Non-sea-salt sulfate concentrations were calculated from  $\text{Na}^+$  concentrations and the ratio of sulfate to sodium in seawater. Sea-salt aerosol concentrations were calculated as

$$\text{sea salt}(\mu\text{g m}^{-3}) = \text{Cl}^-(\mu\text{g m}^{-3}) + \text{Na}^+(\mu\text{g m}^{-3}) \times 1.47, \quad (1)$$

where 1.47 is the seawater ratio of  $(\text{Na}^+ + \text{K}^+ + \text{Mg}^{+2} + \text{Ca}^{+2} + \text{SO}_4^{2-} + \text{HCO}_3^-)/\text{Na}^+$  [Holland, 1978]. This approach prevents the inclusion of non-sea-salt  $\text{K}^+$ ,  $\text{Mg}^{+2}$ ,  $\text{Ca}^{+2}$ ,  $\text{SO}_4^{2-}$ , and  $\text{HCO}_3^-$  in the sea-salt mass and allows for the loss of  $\text{Cl}^-$  mass through  $\text{Cl}^-$  depletion processes. It also assumes that all measured  $\text{Na}^+$  and  $\text{Cl}^-$  is derived from seawater. Results of Savoie and Prospero [1980] indicate that soil dust has a minimal contribution to measured soluble sodium concentrations.

[17] Sources of uncertainty in the ionic mass include the IC analysis, extract liquid volume, and the air volume. The overall uncertainty in the ionic mass at the 95% confidence level, propagated as a quadratic sum of all errors involved, was  $\pm 11\%$  for a concentration of 10  $\mu\text{g m}^{-3}$ . Details of the uncertainty analysis are provided in Quinn *et al.* [2000a].

### 2.2.3. Organic and Elemental Carbon

[18] Details of the substrates and denuders that were used and sample handling procedures are given by Bates *et al.*

[2004]. The submicron OC data are based on a submicron impactor downstream of a denuder. Submicron EC data are the average of two submicron impactor samples (one with and one without a denuder upstream). The supermicron OC data are the difference between sub-10  $\mu\text{m}$  and submicron impactors run without denuders. Impactors without denuders upstream were used for the supermicron OC determination in order to avoid losses of large particles in the denuder. OC concentrations from both impactors were corrected for blanks and artifacts using the last quartz filter in line. Supermicron EC data are the difference between the sub-10  $\mu\text{m}$  and the average of the two submicron impactor samples (with and without denuders). OC and EC concentrations were determined with a Sunset Labs thermal/optical analyzer [Birch and Cary, 1996]. Details of the thermal program can be found in the work of Bates *et al.* [2004].

[19] Size distributions of OC and EC were obtained from seven-stage impactors. The stage 1 quartz filter was corrected for blanks and artifacts using a backup quartz filter. The optical OC/EC split based on the thermal analysis with an optical correction for charred organics works only on the quartz filters and not on the aluminum foils in the impactor. Therefore the OC/EC split for the impactor foils was based on a cruise average EC/TC split of  $0.20 \pm 0.06$  from the quartz filter in the two stage impactors.

[20] No correction was made for carbonate carbon so OC includes both organic and carbonate carbon. The carbonate carbon was never more than 10% of the total OC, however. On the basis of an interlaboratory comparison of punches from four high-volume samples and two blanks, the agreement between eight Sunset Labs carbon analyzers was within 4% for moderate level OC, within 13% for low-level OC, and within 13% for EC [Schauer *et al.*, 2003].

[21] The mass of particulate organic matter (POM) was determined by multiplying the measured OC concentration in  $\mu\text{g m}^{-3}$  by a factor of 2.1 in the marine region and 1.6 elsewhere. The POM factor is an estimated average of the molecular weight per carbon weight and is based on a review of published measurements of the composition of organic aerosol in urban and nonurban regions [Turpin and Lim, 2001]. On the basis of the range of values given by Turpin and Lim [2001], the POM factor has an uncertainty of  $\pm 31\%$ .

[22] The uncertainties associated with positive and negative artifacts in the sampling of semivolatile organic species can be substantial [Turpin *et al.*, 1994, 2000]. An effort was made to minimize positive artifacts by using a denuder upstream of the impactor. Negative artifacts may have occurred as a result of the pressure drop across the impactor (9 mb for the  $D_{aero} = 1.1 \mu\text{m}$  impaction plate and 530 mb for the  $D_{aero} = 0.18 \mu\text{m}$  impaction plate). No attempt was made to determine the uncertainties associated with these artifacts since the information to do so was not available.

[23] Sources of uncertainties in the EC mass include the air volume sampled, 2 times the standard deviation of the blank values measured over the course of the experiment, and the precision of the method ( $\pm 13\%$ ) based on the results of Schauer *et al.* [2003]. A quadratic sum of all errors involved yields a 95% uncertainty of  $\pm 24\%$ . Sources of uncertainty in the POM mass include the air volume sampled, 2 times the standard deviation of the blanks

measured over the course of the experiment, the precision of the method based on the results of *Schauer et al.* [2003], and the POM factor. The 95% uncertainty in the POM mass was  $\pm 37\%$  for moderate levels of OC ( $8.6 \mu\text{g C cm}^{-2}$ ).

#### 2.2.4. Inorganic Oxidized Material (Dust)

[24] Total elemental composition (Na, Mg, Al, Si, P, Cl, K, Ca, Ti, V, Cr, Mn, Fe, Ni, Cu, Zn, Ba, As, and Pb) was determined by thin-film X ray primary and secondary emission spectrometry [*Feely et al.*, 1991, 1998]. Submicron and sub-10  $\mu\text{m}$  samples were collected on Teflo filters (1.0  $\mu\text{m}$  pore size) using two- and one-stage impactors, respectively. Supermicron elemental concentrations were determined by the difference between the submicron and sub-10  $\mu\text{m}$  samples. This method of sample collection allows for the sharp size cut of the impactor while collecting a thin film of aerosol necessary for the X-ray analysis. Filters were weighed before and after sample collection as described below.

[25] A component composed of inorganic oxidized material (IOM) was constructed from the elemental data. The IOM most likely was composed of soil dust and/or fly ash. These two components are difficult to distinguish based on elemental ratios. To construct the IOM component, the mass concentrations of Al, Si, Ca, Fe, and Ti, the major elements in soil and fly ash, were combined. It was assumed that each element was present in the aerosol in its most common oxide form ( $\text{Al}_2\text{O}_3$ ,  $\text{SiO}_2$ ,  $\text{CaO}$ ,  $\text{K}_2\text{O}$ ,  $\text{FeO}$ ,  $\text{Fe}_2\text{O}_3$ ,  $\text{TiO}_2$ ) [*Seinfeld*, 1986]. The measured elemental mass concentration was multiplied by the appropriate molar correction factor as follows:

$$[\text{IOM}] = 2.2[\text{Al}] + 2.49[\text{Si}] + 1.63[\text{Ca}] + 2.42[\text{Fe}] + 1.94[\text{Ti}] \quad (2)$$

[*Malm et al.*, 1994; *Perry et al.*, 1997]. This equation includes a 16% correction factor to account for the presence of oxides of other elements such as K, Na, Mn, Mg, and V that are not included in the linear combination. In addition, the equation omits K from biomass burning by using Fe as a surrogate for soil K and an average K/Fe ratio of 0.6 in soil [*Cahill et al.*, 1986].

[26] Sources of uncertainty in the IOM mass concentration include the X-ray analysis, blank approximation, the volume of air sampled, and the molar correction factor. The overall uncertainty in the IOM mass, propagated as a quadratic sum of all errors involved, was  $\pm 6\%$  for a concentration of  $70 \mu\text{g m}^{-3}$ .

[27] Samples from the seven-stage impactors (used for the calculation of aerosol density, refractive index, and scattering) were analyzed by Inductively Coupled Plasma Mass Spectrometry (ICP-MS) and Atomic Absorption Spectrometry (AA) [*Arimoto et al.*, 2002].

#### 2.2.5. Aerosol Mass

[28] Submicron and supermicron aerosol mass concentrations were determined by weighing the XRF Teflo filters before and after sample collection at a humidity of  $55 \pm 5\%$ . Details of the weighing procedure are provided by *Quinn and Coffman* [1998].

[29] Sources of uncertainty in the aerosol mass include weighing, storage and transport, and the volume of air

sampled. The uncertainty at the 95% confidence level was  $\pm 11\%$  for a mass concentration of  $20 \mu\text{g m}^{-3}$ .

### 2.3. Scattering and Hemispheric Backscattering Coefficients

[30] Measurements of aerosol scattering ( $\sigma_{\text{sp}}$ ) and hemispheric backscattering coefficients ( $\sigma_{\text{bsp}}$ ) were made with an integrating nephelometer (Model 3563, TSI Inc.) at 35 W lamp power setting and wavelengths of 450, 550, and 700 nm at  $55 \pm 5\%$  RH. The RH was measured in the center of the nephelometer sensing volume using a custom installed capacitive type RH sensor (Vaisala model HMP135Y). Two single-stage impactors, one with a  $D_{50,\text{aero}}$  of 1.1  $\mu\text{m}$  and one with a  $D_{50,\text{aero}}$  of 10  $\mu\text{m}$  were placed upstream of the nephelometer. An automated valve switched between the two impactors every 15 min so that sampling alternated between sub-1  $\mu\text{m}$  and sub-10  $\mu\text{m}$  aerosol. Values measured directly by the nephelometer were corrected for an offset determined by measuring filtered air over a period of several hours [*Anderson and Ogren*, 1998]. In addition, submicron and supermicron values were corrected separately for angular nonidealities of the nephelometer, including truncation errors and non-Lambertian illumination, using the method of *Anderson and Ogren* [1998]. Values are reported at  $0^\circ\text{C}$  and 1013 mb.

[31] Sources of uncertainties associated with the use of the integrating nephelometer include photon counting during measurement, zeroing, and calibration; literature values of calibration gas scattering coefficients; variations in gas density within the nephelometer, and the angular correction. These uncertainties were estimated using the method of *Anderson et al.* [1999]. Additional uncertainties include variations in measured scattering due to RH changes within the nephelometer sensing volume and inlet losses of large particles [*Quinn and Coffman*, 1998]. For a 30 min averaging time and a wavelength of 550 nm, a quadrature sum of errors yielded relative uncertainties of  $\pm 14\%$  at the 95% confidence interval.

### 2.4. Absorption Coefficient

[32] The absorption coefficient for submicron and sub-10  $\mu\text{m}$  aerosol,  $\sigma_{\text{ap}}$ , was measured at  $55 \pm 5\%$  RH by monitoring the change in transmission through a filter with a Particle Soot Absorption Photometer (PSAP, Radiance Research). The PSAP was downstream of the same impactors as the nephelometer. Measured values were corrected for a scattering artifact, the deposit spot size, the PSAP flow rate, and the manufacturer's calibration as per *Bond et al.* [1999]. Values are reported at a wavelength of 550 nm,  $0^\circ\text{C}$ , and 1013 mb. Sources of uncertainty in the PSAP measurement include noise, drift, correction for the manufacturer's calibration, and correction for the scattering artifact [*Anderson et al.*, 1999]. A quadrature sum of these errors yielded relative uncertainties of  $\pm 22\%$  for an absorption coefficient of  $10 \text{ Mm}^{-1}$  and a 30 min averaging time.

### 2.5. Size Distributions

[33] Size distributions from 20 nm to 10  $\mu\text{m}$  diameter were measured with the combination of a differential mobility particle sizer (DMPS, University of Vienna (Reischle) medium length column) and an aerodynamic particle sizer (APS). Both instruments were operated at

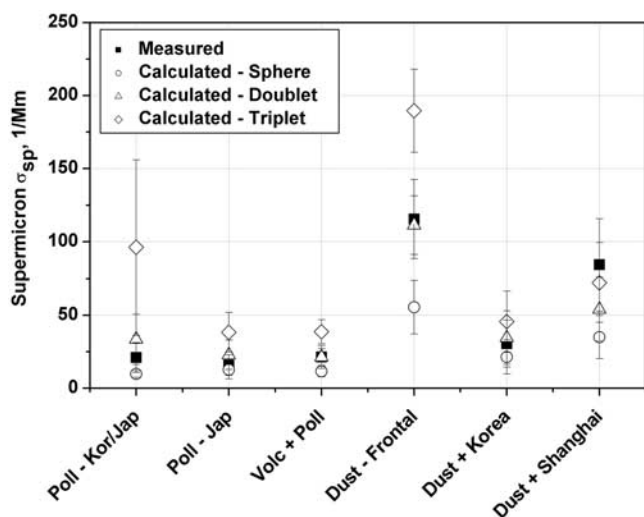


**Figure 2.** Regional mean and  $1\sigma$  standard deviation of the supermicron scattering coefficient (550 nm and 55% RH) as measured by the integrating nephelometer (not corrected for angular nonidealities) and calculated from the supermicron number size distribution as measured with the APS and assuming spherical, doublet (aggregate of two spherical particles), or triplet (aggregate of three spherical particles) shape factors.

$55 \pm 10\%$  RH. Details of the size distribution measurements can be found in the work of *Bates et al.* [2004]. DMPS scans were started every 15 min and lasted about 13 min. Uncertainties in the DMPS-measured size distribution include instrumental errors of particle sizing ( $\pm 5\%$ ) and counting ( $\pm 10\%$ ) due to flow instabilities.

[34] The APS data were measured in 51 size bins with the nominal manufacturer's aerodynamic diameters ranging from 0.542 to 20  $\mu\text{m}$ . Data in the largest four channels (16–20  $\mu\text{m}$ ) were not included in the analysis as it was assumed they were the result of phantom counts. Number size distributions were collected every 15 min and matched to the DMPS scan time.

[35] *Wang and John* [1987] summarized the effect of non-Stokesian conditions and particle density on the APS response to particle aerodynamic diameter. *Cheng et al.* [1990] extended this analysis to include particle shape and the slip correction factor through the following relationship:

$$\frac{\chi(1 + a_2 \text{Re}_{p2}^{b2})}{\rho_{p2} D_{p2}^2 C(D_{p2})} = \frac{(1 + a_1 \text{Re}_{p1}^{b1})}{\rho_{p1} D_{p1}^2 C(D_{p1})}, \quad (3)$$

where subscript 1 refers to a spherical calibration particle and 2 to the particle of interest. Knowing the diameter and density of the spherical calibration particle ( $D_{p1}$  and  $\rho_{p1}$ ), the volume-equivalent diameter of the nonspherical sample particle ( $D_{p2}$ ) can be calculated with knowledge of its density ( $\rho_{p2}$ ), the dynamic shape factor ( $\chi$ ), and ultra-Stokesian correction ( $1 + a_2 \text{Re}_{p2}^{b2}$ ).  $\text{Re}_p$  is defined as

$$\text{Re}_p = \frac{\rho_g D_p (v_g - v_p)}{\eta}, \quad (4)$$

where  $\rho_g$  is the density of air,  $D_p$  is the particle volume-equivalent diameter or  $\sqrt[3]{6V/\pi}$ ,  $v_g$  is the air speed in the instrument,  $v_p$  is the speed of the accelerated particle, and  $\eta$  is the viscosity of air. The APS data were corrected for nonspherical particle shape and ultra-Stokesian conditions using equation (3) and the dynamic shape factor and ultra-Stokesian correction of *Cheng et al.* [1993]. The *Cheng et al.* [1993] measurements included calibration with polystyrene latex (PSL) spheres and nonspherical particles consisting of either two or three aggregated PSL spheres (doublets and triplets, respectively). Figure 2 shows the average and  $1\sigma$  standard deviation of the measured supermicron light scattering for each region as well as the calculated regional scattering coefficient assuming shape factors corresponding to a single sphere, doublet aggregate, or a triplet aggregate.

[36] A multiple linear regression of supermicron mass fractions of the dominant chemical components was used to determine which shape factors (sphere, doublet, or triplet) to use for the different source regions. The lowest mass fractions of dust led to a spherical assumption. Medium and highest mass fractions led to doublet and triplet assumptions, respectively. On the basis of this analysis (which was supported by the supermicron mass and scattering closure) the following shape factors were used: Sphere – Poll-Kor/Jap and Volcano + Polluted; Doublet – Poll-Jap and Dust-Frontal; Triplet – Dust + Korea and Dust + Shanghai. Uncertainties in the APS-measured size distribution include particle sizing ( $\pm 3\%$ ), the instrumental counting efficiency ( $\pm 5\%$ ), and the shape factor ( $\pm 17\%$  for a doublet and  $\pm 22\%$  for a triplet). The error in the shape factor was based on the percent change in size resulting from its use and, hence, most likely is an upper bound.

[37] In order to combine the DMPS and APS size distributions, the APS aerodynamic diameters were converted to geometric diameters using densities calculated with the thermodynamic equilibrium model AeRho [*Quinn and Coffman*, 1998]. See section 3 for a description of the density calculations.

## 2.6. Aerosol Optical Depth

[38] Several instruments were deployed on RHB to determine aerosol optical depth including two hand held Microtops Sun photometers (380, 440, 500, 675, 870 nm) (Solar Light Co.) [*Porter et al.*, 2001], a hand held SIMBAD Sun photometer (443, 490, 560, 670, 870 nm) [*Deschamps et al.*, 2004], and a marine Fast-Rotating Shadow-band Radiometer (FRSR) (410, 500, 615, 680, 870 nm) [*Reynolds et al.*, 2001]. The resulting data have been compared and combined into a “best estimate” time series of AOD by M. A. Miller et al. (Marine Sun photometry using complementary techniques, submitted to *Applied Optics*, 2004, hereinafter referred to as Miller et al., submitted manuscript, 2004). Calibration, data collection, and comparison information for these instruments can be found in Miller et al. (submitted manuscript, 2004).

[39] AOD derived from the four instruments discussed above were compiled to make the most complete data set possible. Regional averages and  $1\sigma$  standard deviations were calculated from the compiled data set. Average values from each instrument were weighted equally so that larger

data sets did not bias the resulting regional AODs. The uncertainty associated with the “consensus” AOD values is  $\pm 0.03$  (Miller et al., submitted manuscript, 2004). Ångström exponents from the regionally averaged AOD were then determined from a linear fit of  $\ln(\text{wavelength})$  versus  $\ln(\text{AOT})$ . The three wavelengths from each instrument nearest to those of the nephelometer (450, 550, 700 nm) were used in this analysis.

### 2.7. Aerosol Vertical Profiles

[40] A micropulse lidar (MPL) system (523 nm) was used to determine vertical profiles of aerosol  $180^\circ$  backscatter and extinction during ACE-Asia [Spinhrne et al., 1995; Welton et al., 2002]. The MPL was situated forward of the vessel's stacks to limit any influence from the ship's engine exhaust, and was housed inside a climate controlled sea container. Raw MPL data were acquired at 1 min time resolution and 75 m vertical resolution. The raw data were converted into uncalibrated lidar signals [Campbell et al., 2002; Welton and Campbell, 2002] and used to infer the altitude of aerosol and cloud heights. Aerosol extinction profiles were calculated for times coincident with Microtops AOT measurements using the algorithm described by Welton et al. [2000].

### 2.8. Meteorological Parameters

[41] Also measured were meteorological parameters including surface temperature, RH, wind speed and direction, as well as vertical profiles of these parameters from radiosondes. Air mass back trajectories were calculated for three arrival altitudes (500, 2500, and 5500 m) for the ship's position at six hour intervals. In cases where a temperature inversion occurred at a sub-500 m height (Polluted – Japan and Volcano + Polluted), additional trajectories were calculated for 50 and 100 m arrival heights. Trajectories were calculated with the hybrid single-particle Lagrangian integrated model HY-SPLIT 4 based on the FNL global wind field [Draxler, 1992] (<http://www.arl.noaa.gov/ready/hysplit4.html>).

## 3. Model Calculations

### 3.1. Calculation of Aerosol Water Mass, Density, and Refractive Index

[42] For the calculation of mass fractions of the aerosol chemical components, the chemical thermodynamic equilibrium model AeRho was used to estimate the water mass associated with the inorganic ions at 55% RH [Quinn and Coffman, 1998; Quinn et al., 2002]. AeRho assumes the inorganic aerosol is an internal mixture containing all measured chemical components. The chemical reactions allowed to occur, the crystallization humidities used for the solid phase species, and the method for the calculation of the aerosol water content are given in Quinn et al. [2002].

[43] Both the IOM and organic mass were assumed to not take up any water. This assumption is supported by the results of a thermodynamic equilibrium model [Ming and Russell, 2002] used to estimate hygroscopic growth factors of the organic-electrolyte mixtures measured in ACE-Asia RHB samples.

[44] Using measured information on organic functional groups and concentrations of inorganic ions and dust, the

Ming and Russell [2002] model was used to calculate hygroscopic growth factors assuming that the organic species were either soluble or insoluble. For both cases the inorganic species were assumed to be in metastable equilibrium, the condition most similar to that in the aerosol instrumentation since the sample air is dried to 55% RH as it is drawn through the inlet [Carrico et al., 2003]. The functional groups that composed the organic mass were determined from submicron aerosol samples collected on Teflon filters on board RHB and analyzed using a Fourier transform infrared (FTIR) spectroscopy technique [Maria et al., 2003]. A model organic mixture was calculated for each sample by minimizing the absolute error between the measured hexane-, dichloromethane-, acetone-, and water-soluble mass fractions of the atmospheric organic matter and the corresponding modeled soluble fractions of a mixture of four compounds: oxalic acid, adipic acid, citric acid, and n-nonadecane. Inorganic compounds were modeled using published solubility and surface tension data. Dust species from XRF analysis, EC from thermal-optical analysis, and carbonate from FTIR analysis were all assumed to be completely insoluble in water [Desboeufs et al., 2001; Chughtai et al., 1996].

[45] The difference in the growth factor defined as  $D_p(55\% \text{ RH})/D_p(\text{dry})$  for the case with soluble organics compared to the case with all organics assumed to be water insoluble is on average +0.5% and, at most, +3.3%, as shown in Figure 3. At 90% RH, the difference in the growth factor for the two cases increases to an average of +2.3% and a maximum of +8.3%. The contribution of the organic fraction of aerosol mass to water uptake for the ACE-Asia aerosol was small due to the low organic aerosol mass fractions (from 8 to 30%) and the low hygroscopicity of the organic functional groups that were present. Hence for the ACE-Asia aerosol, the predicted water uptake is insensitive to the assumptions about the water solubility of the organic fraction. Also shown in Figure 3 is a comparison of ACE-Asia growth factors in which water-soluble organics are neglected calculated by the Ming and Russell [2002] model and calculated by AeRho. The agreement is within a few percent, showing consistency between the two models.

[46] Using the aerosol chemical composition measured with the seven-stage impactors, AeRho also was used to calculate the density and aerosol refractive index at 550 nm using two different approaches. In the first, the aerosol was assumed to an internal mixture containing all measured chemical components and a single bulk density and refractive index was calculated as a function of particle size as described below. In the second approach, density and refractive index were calculated for each chemical component as a function of particle size. The two approaches were found to agree within  $\pm 20\%$  for the submicron size range and  $\pm 40\%$  for the supermicron size range.

[47] Polynomial fits based on data of Tang and Munkelwitz [1991, 1994] for metastable particles were used to estimate densities of individual inorganic soluble species. Data from Bray [1970] were used to estimate the density of  $\text{H}_2\text{SO}_4$ . The density of OC was assumed to be  $1.4 \text{ g cm}^{-3}$  [Turpin and Lim, 2001] and that of EC  $2 \text{ g cm}^{-3}$  [Bergstrom, 1972]. The density of the IOM component was set equal to that of a mixture of illite and hematite with the fraction of hematite based on the measured Fe concentrations. For the bulk density calculations, a volume weighted average was taken

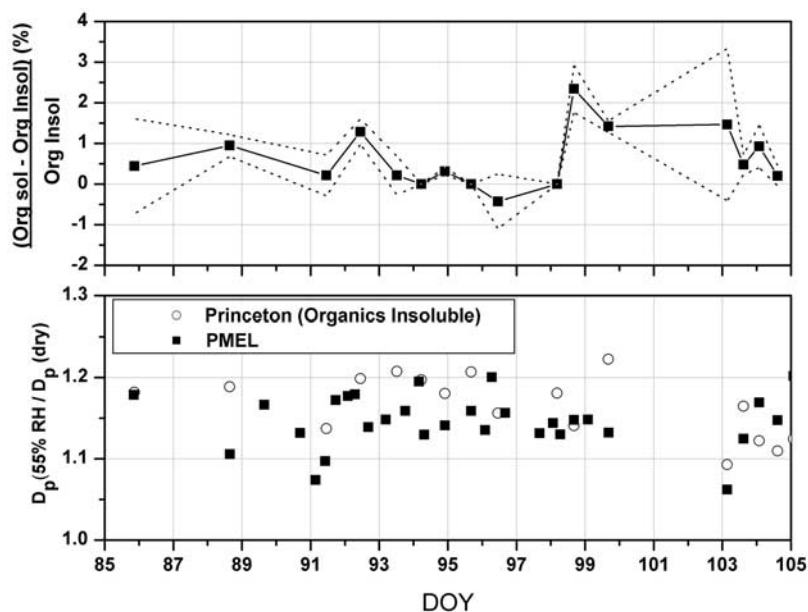


**Figure 3.** (top) Percent difference in the hygroscopic growth factor ( $D_p(55\% \text{ RH})/D_p(\text{dry})$ ) calculated assuming organic species are soluble and insoluble. These growth factors were calculated by the thermodynamic equilibrium model of *Ming and Russell* [2002]. Black squares were calculated using organic solubility data from an FTIR solvent-rinsing process [*Maria et al.*, 2002]. The upper and lower dotted lines represent the most hygroscopic and the most hydrophobic organic compositions that fall within the uncertainties of the FTIR solvent-rinsing procedure, respectively. (bottom) Comparison of the *Ming and Russell* [2002] and PMEL growth factors calculated with AeRho. In all cases, the inorganic species are assumed to be in metastable equilibrium.

of the density of the individual species to estimate the density of the aerosol mix in each impactor size bin. Average submicron and supermicron densities for each source region for the mix of aerosol chemical components are reported in Table 1. For the single component density calculations, the density of that component was used. If the component was made up of several chemical species, which was the case for sulfate and sea salt, the volume weighted average of the densities of the species making up that component were used. For example, for the sulfate component, the density was the volume weighted average density for the relative amounts of  $\text{H}_2\text{SO}_4$ ,  $\text{NH}_4\text{HSO}_4$ , and  $(\text{NH}_4)_2\text{SO}_4$  calculated to exist in each size bin.

[48] For the bulk aerosol, the method of partial molar refractions [*Stelson*, 1990] was used to calculate the real portion of the refractive index as a function of size at a wavelength of 550 nm. Values of the partial molar refractions of all chemical species except IOM were taken from

[*Stelson*, 1990]. The complex refractive index at 550 nm was obtained by volume averaging the refractive index of the scattering and absorbing components. Refractive indices of  $1.56-0.001i$  and  $2.89-0.512i$  were used for the illite and hematite, respectively, in the IOM (Dust) mixture at 550 nm [*Sokolik and Toon*, 1999]. Average submicron and supermicron refractive indices for each source region for the mix of aerosol chemical components are reported in Table 1. For the single chemical components, the refractive index of that component was used. If the chemical component contained more than one molecular species (sulfate and sea salt), as determined by AeRho, the method of partial molar refraction was used.

### 3.2. Calculation of Scattering due to the Total Aerosol and to Each Chemical Component

[49] The chemical components considered in this analysis are sea salt, nss sulfate, IOM (Dust), POM, and EC. The

**Table 1.** Regional Averages and  $1\sigma$  Standard Deviation of Submicron ( $D_{\text{aero}} < 1.1 \mu\text{m}$ ) and Supermicron ( $1.1 < D_{\text{aero}} < 10 \mu\text{m}$ ) Densities and Real and Imaginary Portions of the Refractive Index of the Bulk Aerosol Estimated From the Chemical Thermodynamic Equilibrium Model, AeRho<sup>a</sup>

Region	Density, $\text{g cm}^{-3}$		Refractive Index, Real Portion		Refractive Index, Imaginary Portion	
	Sub-1 $\mu\text{m}$	Supermicron	Sub-1 $\mu\text{m}$	Supermicron	Sub-1 $\mu\text{m}$	Supermicron
Polluted – Korea/Japan	$1.42 \pm 0.01$	$1.63 \pm 0.12$	$1.48 \pm 0.01$	$1.48 \pm 0.01$	$0.02 \pm 0.01$	0
Polluted – Japan	$1.44 \pm 0.02$	$1.91 \pm 0.09$	$1.49 \pm 0.01$	$1.51 \pm 0.01$	$0.02 \pm 0.02$	$0.02 \pm 0.01$
Volcano + Polluted	$1.42 \pm 0.01$	$1.72 \pm 0.13$	$1.48 \pm 0.005$	$1.50 \pm 0.03$	$0.01 \pm 0.01$	$0.01 \pm 0.01$
Dust – Frontal	$1.65 \pm 0.17$	$2.47 \pm 0.18$	$1.50 \pm 0.02$	$1.57 \pm 0.02$	$0.02 \pm 0.01$	$0.01 \pm 0.01$
Dust + Korea	$1.75 \pm 0.17$	$2.57 \pm 0.17$	$1.55 \pm 0.01$	$1.60 \pm 0.02$	$0.02 \pm 0.02$	$0.02 \pm 0.01$
Dust + Shanghai	1.51	2.36	1.49	1.56	0.03	0.02

<sup>a</sup>Values are reported for 55% RH and 550 nm.

**Table 2.** Air Mass Classification and Source Region<sup>a</sup>

Classification/Source Region	Region No.	Ship Location	Trajectories	Comments
Marine/North Pacific, 75–84 (DOY)	1	Hawaii to 165°E	500 m: North Pacific; 2500 m: N. China/Mongolia dust region; 5500 m: N. China to Korea and Japan.	BLH from 1 to 2 km with several weak midlatitude low-pressure disturbances (DOY 76, 80, and 83). RH 55 to near 100%.
Polluted/Korea/Japan, 91–94	2	south coast of Japan	500 m: N. China to Korea and/or Japan; 5500 m: N. China/Mongolia dust region (DOY 92.25).	BLH 1 to 2 km at beginning and end of period. Up to 8 km in the middle of the period. RH 45 to 70%.
Polluted/Japan, 96.4–99.2	3	Sea of Japan	50, 100, and 500 m: Air circulating over Japan for several days; 2500 and 5500 m: N. China/Mongolia dust region.	Relatively low seawater temperatures (7°–13°C). Strong temperature inversion throughout the period, resulting in a shallow mixed layer with a height of 100–400 m. High RH (75 to 95%).
Volcano + Polluted, 99.3–100.5	4	Sea of Japan	50, 100, and 500 m: China to Japan and Miyakejima volcano; 2500 and 5500 m: N. China/Mongolia dust region.	Relatively low seawater temperatures (10°–14°C). Strong temperature inversion. Shallow mixed layer (<200 m). High RH (85–95%).
Dust – Frontal Passage, 101–101.3	5	western Sea of Japan	500 m: China to Korea; 2500 m: N. China/Mongolia dust region.	Frontal passage began at 100.8. Well-mixed atmosphere up to about 10 km. RH 80 to 92%.
Dust + Korea, 101.8–103.4	6	southern Sea of Japan	500 and 2500 m: N. China/Mongolia dust region to Korea.	Low RH (35–60%). BLH 1–3 km.
Dust + Shanghai, 103.4–104.5	7	Korean Strait	500 and 2500 m: N. China/Mongolia dust region to Shanghai.	RH variable (55–80%). BLH 0.5–3.5 km.

<sup>a</sup>Region numbers correspond to those in Figure 1. BLH, boundary layer height; RH, ambient relative humidity.

sea-salt component includes all measured  $\text{NO}_3^-$  in the supermicron size range on the assumption that gas-phase  $\text{HNO}_3$  resulting from combustion processes reacts with sea salt to form  $\text{NaNO}_3$  [Clegg and Brimblecombe, 1985]. Non-sea-salt sulfate aerosol includes nss  $\text{SO}_4^{2-}$  and all measured  $\text{NH}_4^+$  up to an  $\text{NH}_4^+$  to nss  $\text{SO}_4^{2-}$  molar ratio of 2. The sea-salt and nss sulfate components also include the water calculated to be associated with these components at 55% RH.

[50] Size distributions of sea salt, nss sulfate aerosol, POM, and EC were determined from the seven-stage impactor measurements coupled with the number size distributions. Using the calculated density from  $\text{AeRho}$ , a volume ratio (component volume/total aerosol volume) was calculated for each component within each impactor size bin. From this, component surface area size distributions were derived. This approach uses the measured chemical information but maintains the higher size resolution of the measured number size distribution. Scattering coefficients were calculated using a Mie theory model based on Bohren and Huffman's BHMIE code [Bohren and Huffman, 1983]. Bulk aerosol refractive indices were used for the calculation of scattering by the total aerosol. Single component refractive indices were used for the calculation of scattering by the individual chemical components.

[51] The effect of nonspherical particle shape was incorporated into the scattering calculations by using the APS size distributions corrected with a dynamic shape factor for either doublet or triplet agglomerates of spherical particles (see section 2.5). This approach assumes that scattering due to supermicron nonspherical particles can be estimated from doublet or triplet agglomerates of spherical particles that have the same surface-equivalent diameter as the nonspherical particles. This assumption is supported by the compu-

tations of Mishchenko *et al.* [1997] which indicate that extinction due to large nonspherical particles is similar to that due to spherical particles with the same surface-equivalent diameter. The uncertainty in the calculated scattering due to the shape factor ( $\pm 33\%$  for a doublet and  $\pm 40\%$  for a triplet) was based on the percent change in scattering resulting from its use.

[52] Having acquired size distributions of  $\sigma_{\text{sp}}$  for each component, values of submicron, supermicron, and sub-10  $\mu\text{m}$  component  $\sigma_{\text{sp}}$  values were determined by integrating over the appropriate size range. Mass scattering efficiencies ( $\text{m}^2 \text{g}^{-1}$ ) were calculated from the component scattering,  $\sigma_{\text{sp},j}$  ( $\text{Mm}^{-1}$ ), and mass concentrations ( $\mu\text{g m}^{-3}$ ) for the submicron, supermicron, and sub-10  $\mu\text{m}$  size ranges.

## 4. Results

### 4.1. General Meteorology and Air Mass Source Regions

[53] Presented here is a general overview of the meteorological conditions encountered on RHB during ACE-Asia. A detailed list of the air mass classifications and source regions are shown in Table 2. Trajectories typical of each source region and RHB cruise track are shown in Figure 1.

[54] Marine air (defined as the 500 m trajectories not being over land for at least 5 days prior to reaching the ship) was sampled during the first 10 days of the transit from Hawaii to Japan (DOY 75 to 84, 16–25 March). On DOY 81 (22 March), however, the 500 m trajectories remained marine but the 2500 m trajectories indicated flow from the N. China/Mongolia dust region and the 5500 m trajectories indicated flow from N. China to Korea and Japan.

[55] Once the ship was about 2000 km downwind of Japan (DOY 84), trajectory analysis indicates that air masses traveling from the west were encountered that had passed over nearby continental regions. From DOY 88 to 96 (29 March–6 April), a series of frontal systems moved eastward through the ACE-Asia region. No observations of dust at the surface were reported in the regional daily weather maps. The surface aerosol was composed of pollutants arriving from Korea and/or Japan and also was influenced by the Miyakejima volcano.

[56] On DOY 97 (7 April) the situation changed as a low-pressure center located east of Lake Baikal lofted dust to the upper troposphere. From DOY 97 to 100 (7–10 April), the ship remained ahead of the frontal system and sampled dust that arrived at the surface via subsidence. During this period, lower-level trajectories (50, 100, and 500 m) indicated the sampled air had circulated over Japan for several days before reaching the ship. Upper level trajectories (2500 and/or 5500 m) indicated flow from the direction of the Taklamakan and Gobi deserts. A strong temperature inversion persisted throughout this period resulting in a shallow mixed layer with a height of 0.1 to 0.4 km. The boundary layer aerosol was primarily composed of pollution and volcanic emissions from Japan with dust making up a relatively small fraction of the aerosol mass.

[57] On DOY 100.8 (10 April), the frontal system passed over the ship. Initially on DOY 101, the 500 m trajectories indicated flow from China and Korea while the 2500 m trajectories indicated flow from the Mongolia/N. China dust region. The aerosol was a mixture of pollution and dust. Following the frontal passage, later on DOY 101 to 103 (11–13 April), both the lower and upper level trajectories were from the dust region and dust made up a significant fraction of the submicron aerosol mass and dominated the supermicron aerosol mass. In addition, the height of the well-mixed boundary layer increased to between 1 and 3 km. On DOY 103 (13 April) a low-pressure system developed over northeast China. By DOY 104 (14 April) it had moved eastward over Japan and the location of the ship. During this period, the concentrations of dust measured on the ship remained relatively high. At no time was “pure” dust measured on the ship. It was accompanied by pollutant aerosol from a variety of source regions depending on the transport pathway to the ship.

## 4.2. Closure Tests: Comparison of Measured and Calculated Aerosol Mass and Scattering

### 4.2.1. Mass Closure

[58] Mean regional values of three measures of mass were compared to assess internal consistency in the impactor and number size distribution data used in the scattering calculations. Submicron and supermicron aerosol mass concentrations were determined by gravimetric analysis, by summing the mass of the chemically analyzed species, and from the number size distribution using the density of the aerosol mixture estimated with AeRho. The amount of water calculated to be associated with the aerosol at 55% RH was added to the chemically analyzed mass to adjust it to the measurement RH of the gravimetric analysis and number size distributions. As described in section 2.5., shape factors were included in

the mass derived from the number size distribution to account for the APS response to particle asphericity.

[59] As shown in Figure 4, both the submicron and supermicron mass concentrations from the three methods agreed within the overall experimental uncertainty for all source regions. The overall experimental uncertainty was calculated from a quadrature sum of the uncertainties of the three methods [Quinn and Coffman, 1998]. This level of agreement indicates that the measured mass concentrations of the chemical components and the total aerosol are consistent with the size distributions used in the scattering calculations. Furthermore, it lends confidence to the particle density and associated water calculated by AeRho. At the same time, however, this analysis also indicates the large uncertainties in the supermicron mass estimated from the APS measurements. Even though the correction for particle shape yields closure within experimental uncertainties, it is unsatisfying in that it relies on assumptions about the shape of the particles rather than empirical knowledge.

### 4.2.2. Scattering Closure

[60] Mean regional measured and calculated scattering coefficients are shown in Figure 5 for the submicron and supermicron size ranges. The sources of uncertainty associated with the calculated values are listed and quantified in Table 3. To obtain the most direct comparison of the measured and calculated scattering coefficients, the scattering coefficients measured directly by the nephelometer without any angular correction were compared to those calculated with the nephelometer angular sensitivity function which is based on the actual geometry of the nephelometer’s sensing volume [Heintzenberg, 1978; Anderson *et al.*, 1999]. Hence the uncertainty of the angular truncation corrections is omitted from the comparison. For all regions and both size ranges, the measured and calculated scattering coefficients agree within the overall experimental uncertainty. This agreement lends confidence to the shape factor chosen for each region and to the calculated scattering due to the individual chemical components.

### 4.2.3. Absorption Closure

[61] Regional mean measured and calculated absorption coefficients are shown in Figure 6 for the submicron and supermicron size ranges. Sources of uncertainty associated with the calculated values are listed and quantified in Table 3. Agreement was obtained for the submicron aerosol in four out of six regions and in the supermicron aerosol in all regions. For many of these regions, however, the agreement is barely within the large overall experimental uncertainty. For the submicron size range, the difference in the mean measured and calculated absorption coefficients leads to a difference in single scattering albedo of 0.02 to 0.1 and in the supermicron size range of 0.04 to 0.15. Putting this range of single scattering albedos into perspective, depending on the cloud fraction and surface albedo, a change in single scattering albedo of 0.1 may be sufficient to change the sign of the top of atmosphere (TOA) forcing. It has been estimated that aerosols have a net negative (cooling) versus positive (warming) TOA forcing for single scattering albedos greater than 0.95 and less than 0.85, respectively [Ramanathan *et al.*, 2001]. Also troubling is how systematic the differences were. For every region, measured values were higher than calculated values in the submicron size range and lower in the supermicron size range.

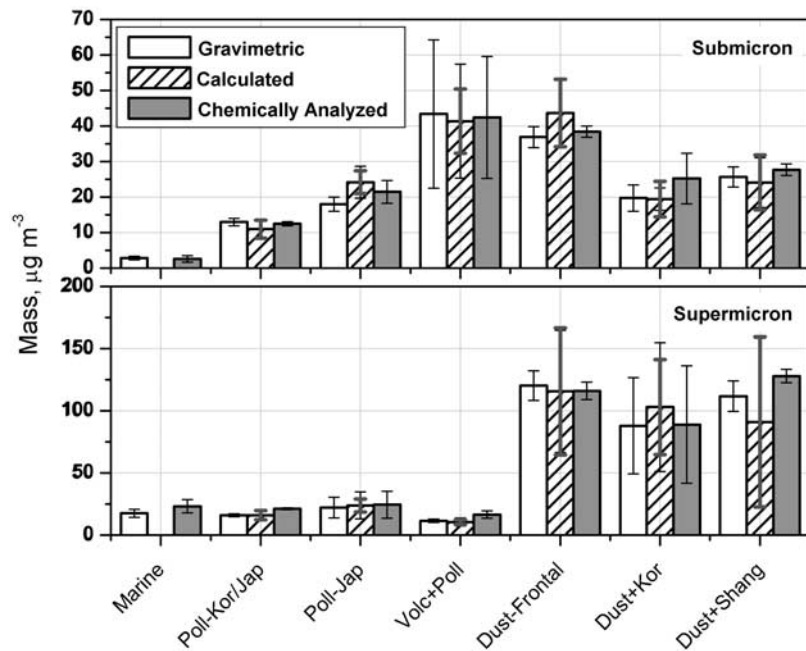


**Figure 4.** Comparison of three measures of the aerosol mass concentration at 55% RH for the submicron and supermicron size ranges. Gravimetric denotes the gravimetrically analyzed mass, and chemically analyzed is the sum of the mass analyzed for inorganic ions, organic (as POM), black carbon, and trace elements (as IOM). The chemically analyzed mass also includes the water calculated to be associated with the inorganic ions at 55% RH. Calculated denotes the mass estimated from the number size distribution and the density based on the measured chemical composition. Black error bars indicate the  $1\sigma$  standard deviation of the mean or, for regions where only one or two samples were collected, the 95% uncertainty. Gray error bars indicate the overall uncertainty at the 95% confidence level for the mass closure experiment.

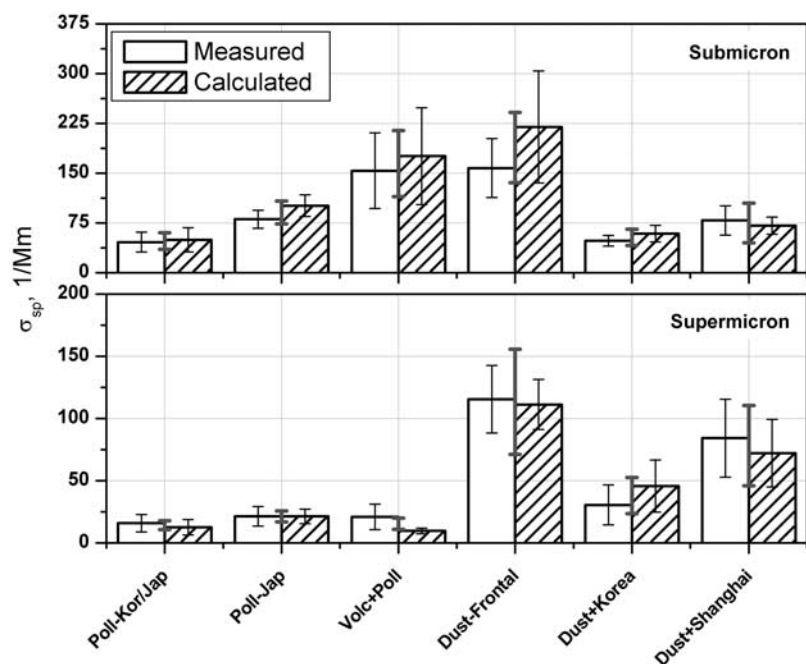


**Figure 5.** Comparison of the regional mean measured scattering (STP but not angular corrected  $\sigma_{sp}$  from the nephelometer) and calculated scattering (nephelometer-simulated  $\sigma_{sp}$ ) for the submicron and supermicron size ranges. All results are shown at 55% RH and 550 nm. Error bars are as in Figure 4.

**Table 3.** Sources of Uncertainty in the Calculated Scattering and Absorption Coefficients

Source of Uncertainty	$\sigma_{sp}$ Relative Uncertainty, %	$\sigma_{ap}$ Relative Uncertainty, %
<i>Sub-1 <math>\mu\text{m}</math></i>		
Number distribution		
Instrumental sizing	$\pm 15$	$\pm 15$
Instrumental counting	$\pm 10$	$\pm 10$
Density and refractive index <sup>a</sup>	$\pm 30$	$\pm 30$
<b>Overall<sup>b</sup></b>	<b><math>\pm 35</math></b>	<b><math>\pm 35</math></b>
<i>Supermicron</i>		
Number distribution		
Instrumental sizing	$\pm 15$	$\pm 15$
Instrumental counting	$\pm 10$	$\pm 10$
Density and refractive index <sup>a</sup>	$\pm 30$	$\pm 30$
Shape correction, doublet <sup>c</sup>	$\pm 36$	$\pm 54$
Shape correction, triplet <sup>c</sup>	$\pm 61$	$\pm 71$
<b>Overall<sup>b</sup></b>	<b><math>\pm 35</math> (sphere)</b>	<b><math>\pm 35</math> (sphere)</b>
	<b><math>\pm 50</math> (doublet)</b>	<b><math>\pm 64</math> (doublet)</b>
	<b><math>\pm 70</math> (triplet)</b>	<b><math>\pm 79</math> (triplet)</b>

<sup>a</sup>On the basis of the uncertainty in the dust refractive index and density.

<sup>b</sup>The overall uncertainty is based on a quadrature sum of the individually listed uncertainties. Hence the sources of uncertainty are assumed to be independent, which may lead to an underestimate of the overall uncertainty.

<sup>c</sup>Assigned uncertainty is the change in scattering (or absorption) resulting from the correction of the APS-measured size distribution with the dynamic shape factor for a doublet or triplet aggregate of spherical particles.

[62] The mass absorption efficiency of EC,  $\alpha_{ap,EC}$ , defined as

$$\alpha_{ap,EC} = \frac{\sigma_{ap,EC}}{m_{EC}}, \quad (5)$$

provides a useful constraint for the Mie calculated absorption coefficient since it has a theoretical limit for a given wavelength, size distribution, and EC density and refractive index. For a wavelength of 550 nm and commonly assumed densities and refractive indices of EC,  $\alpha_{ap,EC}$  does not exceed  $10 \text{ m}^2 \text{ g}^{-1}$  [e.g., Martins *et al.*, 1998; Fuller *et al.*, 1999]. To compare to this theoretical limit, the submicron mass absorption efficiency of elemental carbon was calculated in two different ways. In the first or measurement-based method,  $\sigma_{ap,EC}$  was the PSAP-measured absorption coefficient calculated as per Bond *et al.* [1999] and  $m_{EC}$  was the mass concentration of elemental carbon determined from the thermo-optical carbon analysis of the impactor sample. In the second or calculational method,  $\sigma_{ap,EC}$  was calculated from Mie theory using the measured chemical composition and size distribution as described in section 3 and  $m_{EC}$  was, as before, the measured mass concentration of elemental carbon from the thermo-optical carbon analysis.

[63] Figure 7 shows frequency distributions from the measurement-based and calculational derivations of submicron  $\alpha_{ap,EC}$  for all non-Marine samples collected. Measurement-based values ranged from 5 to  $25 \text{ m}^2 \text{ g}^{-1}$  while the calculation values ranged from 2 to  $8 \text{ m}^2 \text{ g}^{-1}$ . There are several possibilities for the large difference between the measurement-based and calculational values. If the aerosol is well described by Mie theory and the assumption of

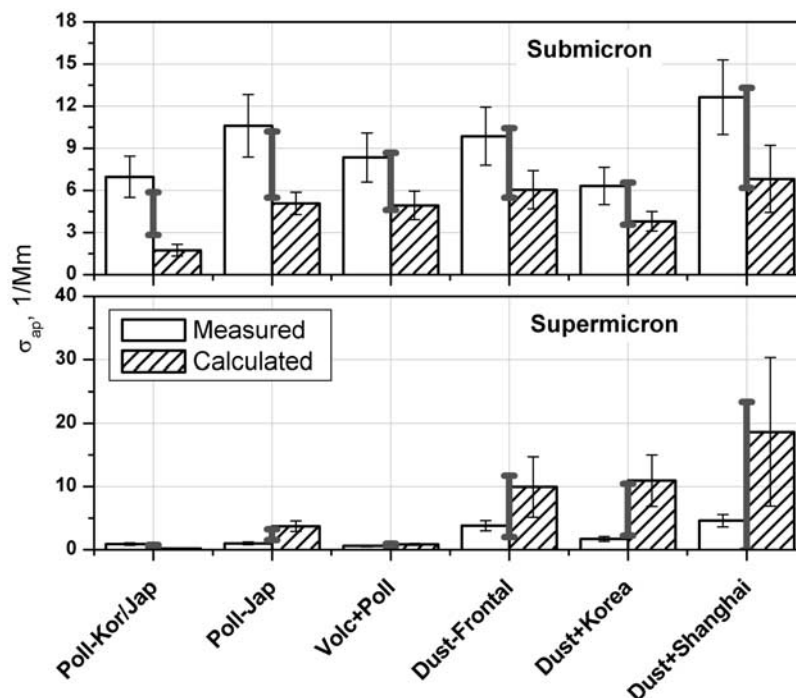


**Figure 6.** Comparison of the regional mean measured and calculated absorption coefficient for the submicron and supermicron size ranges. All results are shown at 55% RH and 550 nm. Error bars are as in Figure 4.

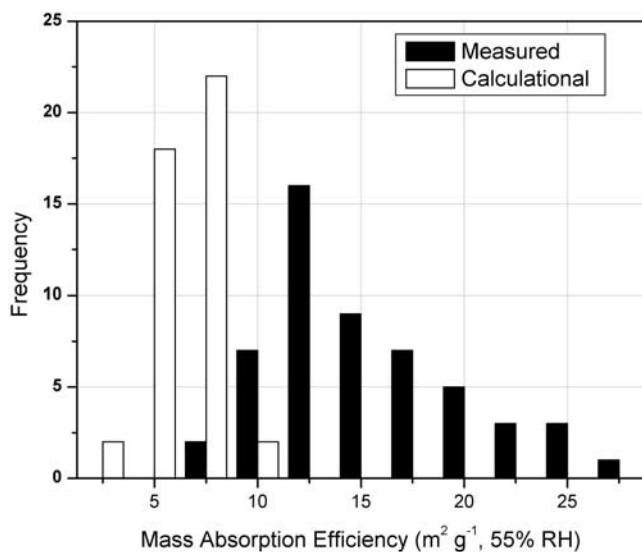


**Figure 7.** Frequency distribution of measurement-based and calculational mass absorption efficiencies for the submicron size range at 550 nm and 55% RH. Measured values were derived from the PSAP-measured absorption coefficient divided by the measured EC mass concentration. Calculational values were derived from the Mie-calculated absorption coefficient divided by the measured EC mass concentration.

individual internally mixed, homogeneous spheres applies, then the large values of  $\alpha_{\text{ap,EC}}$  from the measurement-based method may indicate instrumental issues such as (1) the inability of the thermo-optical technique to accurately measure all midvisible absorbing species present, (2) the difficulty in accurately determining the split point between OC and EC in the thermo-optical analysis, and/or (3) the inability to parameterize the PSAP scattering correction factor with large dust loadings on the filter and/or uncertainty in the filter transmission correction function. A comparison of  $\alpha_{\text{ap,EC}}$  and dust loading did not show any evidence of the latter, however. Alternatively, it may be that the assumption of internally mixed homogeneous single spheres does not accurately describe the absorption by the ACE-Asia elemental carbon. If so, there are implications for the modeling of optical properties of the aerosol using Mie theory and the measurement of the submicron aerosol with a combination of instruments (DMPS + APS) that may not accurately size nonspherical particles [Heintzenberg *et al.*, 2002; Cheng *et al.*, 1993]. Fuller *et al.* [1999] extended Mie theory beyond single carbon spheres and showed that  $\alpha_{\text{ap,EC}}$  can exceed  $10 \text{ m}^2 \text{ g}^{-1}$  by up to a factor of 2.5 to 4 for carbon spheres embedded in host particles having a refractive index between 1.33 and 1.53 and a diameter greater than  $0.4 \mu\text{m}$ .

[64] Unlike the mass and scattering closure experiments, absorption closure was not obtained relative to reasonable limits of uncertainty. In addition, there were systematic differences between the measured and calculated absorption for both the submicron and supermicron size ranges. As a result, we have chosen not to present extinction or absorption due to individual chemical components but instead to focus on component scattering and mass scattering efficiencies. Similarly, we use the measured rather than the modeled

absorption for the calculation of single scattering albedo which is discussed in section 4.5.2.

### 4.3. Aerosol Chemical Composition as a Function of Source Region

[65] Aerosol mass concentrations determined by gravimetric analysis are shown for the sub-, super-, and sub- $10 \mu\text{m}$  size ranges as a function of air mass category in Figure 8.

#### 4.3.1. Submicron Aerosol

[66] Submicron mass concentrations were lowest in the marine region. The average concentration as the ship traveled from Hawaii westward to  $160^\circ\text{E}$  was  $2.8 \pm 0.52 \mu\text{g m}^{-3}$ . As the ship neared the coast of Japan and air mass flow came from Korea and Japan, the average concentration increased by almost a factor of 5 to  $13 \pm 3.7 \mu\text{g m}^{-3}$  (Polluted – Korea/Japan). The average concentration increased again to  $18 \pm 2.0 \mu\text{g m}^{-3}$  as the ship entered the Korean Strait and the Sea of Japan and air circulated over Japan for several days before reaching the ship (Polluted – Japan). Submicron concentrations reached the highest levels measured on the ship ( $43 \pm 21 \mu\text{g m}^{-3}$ ) during a one day period when emissions from the Miyakejima volcano (located 150 km south of Tokyo at  $34.08^\circ\text{N}$  and  $139.53^\circ\text{E}$ ) combined with the pollution from Japan (Volcano + Polluted). A shallow boundary layer ( $<500 \text{ m}$ ) and high RH (85 to 95%) contributed to the high mass concentrations and hazy conditions. Once outbreaks

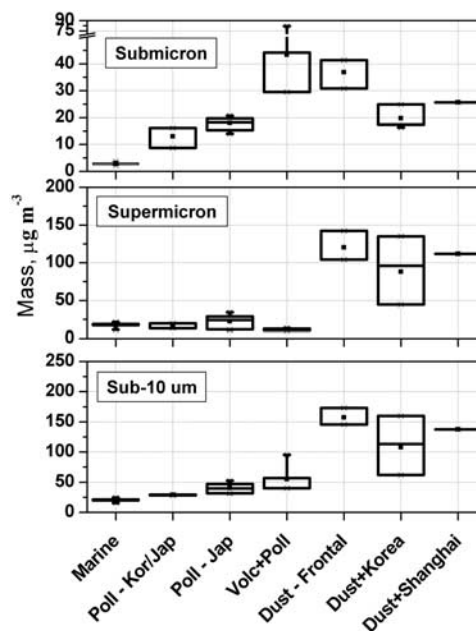


**Figure 8.** Aerosol mass concentration for the submicron, supermicron, and sub- $10 \mu\text{m}$  size ranges for each of the seven regions. Results are reported at  $55 \pm 5\%$  RH. Horizontal lines in the box denote the 25th, 50th, and 75th percentile values. The vertical error bars denote the 5th and 95th percentile values. The two symbols below the 5th percentile bar denote the 0th and 1st percentile, and the two symbols above the 95th percentile bar denote the 99th and 100th percentiles. The square symbol in the box denotes the mean.

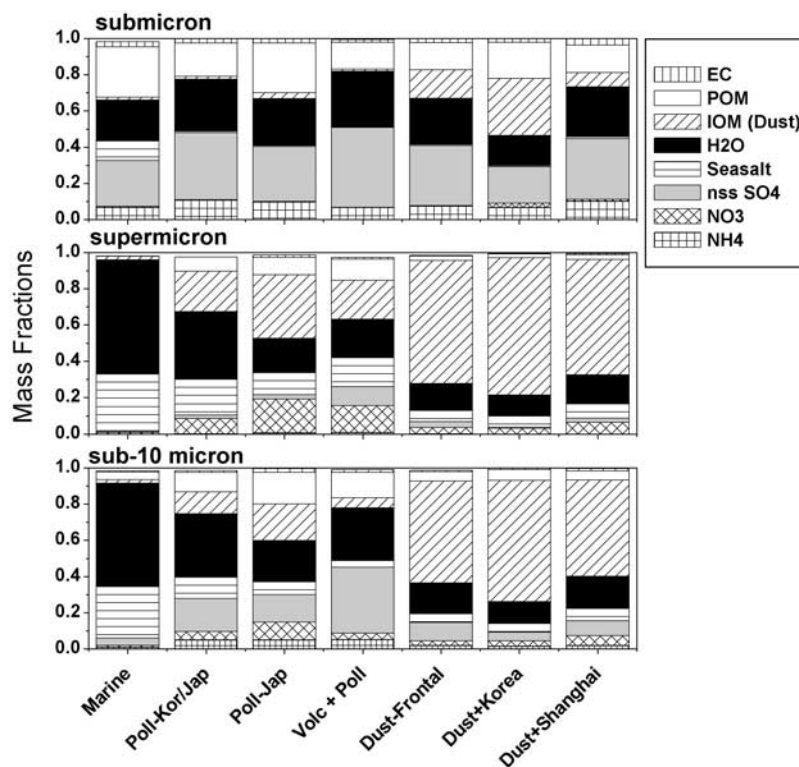


**Figure 9.** Mean regional mass fractions of the dominant chemical components for the submicron, supermicron, and sub-10  $\mu\text{m}$  size ranges. EC refers to elemental carbon, POM to particulate organic matter, and  $\text{H}_2\text{O}$  to the amount of water calculated to be associated with the inorganic ionic species at 55% RH. See color version of this figure in the HTML.

of dust reached the ship on Day 101, submicron mass concentrations remained elevated with average concentrations of  $37 \pm 5.3$ ,  $20 \pm 3.7$ , and  $26 \pm 1.3 \mu\text{g m}^{-3}$  for the Dust – Frontal, Dust + Korea, and Dust + Shanghai regions, respectively.

[67] Mass fractions of the aerosol chemical components were calculated from the gravimetrically analyzed mass and the mass concentrations of the individual components. Mean mass fractions for the submicron, supermicron, and sub-10  $\mu\text{m}$  size ranges are shown in Figure 9 and reported in Table 4. Absolute mass concentrations of the chemical components and the processes controlling them are reported in a companion paper by Bates *et al.* [2004]. In the regions impacted by marine, pollution, and volcanic emissions, the submicron aerosol was composed primarily of ammonium sulfate salts plus associated water and POM. In the marine region there also was a substantial contribution from sea salt. In the three dust regions, dust was a significant component making up, on average, 8 to 31% of the submicron mass. The concentration of dust is based on elemental concentrations of Al, Si, Ca, Fe, and Ti. Since these elements also are present in fly ash generated by combustion of fossil fuels, a portion of the submicron “dust” component may actually be fly ash.

[68] Mean submicron mass fractions of nitrate were 2% or less for all regions. Mean submicron mass fractions of EC were relatively low ranging from 2 to 4%. Highest values were observed in the Dust + Shanghai region but were still only half those observed during INDOEX when

trajectories were from eastern India near Calcutta [Quinn *et al.*, 2002].

#### 4.3.2. Supermicron Aerosol

[69] Two levels of supermicron aerosol mass concentrations were observed. Relatively low concentrations were found in the Marine ( $17 \pm 3.3 \mu\text{g m}^{-3}$ ), Polluted – Korea/Japan ( $16 \pm 3.2 \mu\text{g m}^{-3}$ ), Polluted – Japan ( $22 \pm 8.3 \mu\text{g m}^{-3}$ ), and Volcano + Polluted ( $11 \pm 1.3 \mu\text{g m}^{-3}$ ) regions. The mean wind speeds and supermicron sea-salt concentrations measured during ACE-Asia were similar to those observed during previous campaigns (ACE 2 and INDOEX) [Quinn *et al.*, 2000b; Quinn *et al.*, 2002]. During ACE-Asia, however, these sea-salt concentrations were overwhelmed by the dust concentrations measured in the dust regions. Mean supermicron mass concentrations in the dust regions were  $120 \pm 19 \mu\text{g m}^{-3}$  (Dust – Frontal),  $88 \pm 39 \mu\text{g m}^{-3}$  (Dust + Korea), and  $112 \pm 5.6 \mu\text{g m}^{-3}$  (Dust + Shanghai).

[70] As shown in Figure 9, the supermicron aerosol was composed primarily of sea salt and associated water in the Marine region. In the three polluted regions both sea salt and dust were dominant chemical components. For the dust regions, the average mass fractions of supermicron dust ranged from 64 to 76% indicating the large impact of dust on the aerosol chemistry during the dust events. Sea salt plus associated  $\text{H}_2\text{O}$  made up about 20% of the supermicron mass in the dust regions. Nitrate made up 8 to 18% of the supermicron mass in the polluted regions and 3 to 6% in the dust regions. The almost exclusive presence of nitrate in the supermicron aerosol (with the exception of Dust +

**Table 4.** Average Mass Fractions of the Dominant Aerosol Chemical Components for the Submicron ( $D_{\text{aero}} < 1.1 \mu\text{m}$ ), Supermicron ( $1.1 < D_{\text{aero}} < 10 \mu\text{m}$ ), and Sub- $10 \mu\text{m}$  ( $D_{\text{aero}} < 10 \mu\text{m}$ ) Size Ranges<sup>a</sup>

Component	$\mu\text{g m}^{-3}$						
	Marine	Polluted – Korea/Japan	Polluted/Japan	Volcano + Polluted	Dust – Frontal	Dust + Korea	Dust + Shanghai
<b>No. Samples</b>	<b>4</b>	<b>2</b>	<b>7</b>	<i>Submicron</i> <b>3</b>	<b>2</b>	<b>4</b>	<b>1</b>
NH <sub>4</sub> <sup>+</sup>	0.07 ± 0.01	0.11 ± 0.01	0.10 ± 0.01	0.07 ± 0.02	0.07 ± 0.01	0.07 ± 0.03	0.10 ± 0.005
NO <sub>3</sub> <sup>-</sup>	0.005 ± 0.002	0.002 ± 0.002	0.002 ± 0.001	BDL	0.001 ± 0.001	0.02 ± 0.006	0.01 ± 0.005
nss SO <sub>4</sub> <sup>=</sup>	0.25 ± 0.04	0.37 ± 0.09	0.30 ± 0.02	0.44 ± 0.04	0.33 ± 0.05	0.20 ± 0.04	0.34 ± 0.02
Sea salt	0.11 ± 0.06	0.01 ± 0.002	0.008 ± 0.005	0.003 ± 0.001	0.007 ± 0.004	0.008 ± 0.002	0.01 ± 0.001
H <sub>2</sub> O	0.22 ± 0.03	0.29 ± 0.03	0.26 ± 0.01	0.31 ± 0.06	0.25 ± 0.03	0.16 ± 0.04	0.27 ± 0.01
IOM (dust)	0.01 ± 0.02	0.02 ± 0.01	0.03 ± 0.01	0.01 ± 0.01	0.16 ± 0.12	0.31 ± 0.17	0.08 ± 0.004
POM	0.28 ± 0.05	0.18 ± 0.12	0.27 ± 0.02	0.15 ± 0.06	0.15 ± 0.03	0.20 ± 0.06	0.15 ± 0.01
EC	0.03 ± 0.003	0.02 ± 0.01	0.03 ± 0.01	0.02 ± 0.01	0.02 ± 0.01	0.02 ± 0.005	0.04 ± 0.002
				<i>Supermicron</i>			
NH <sub>4</sub> <sup>+</sup>	BDL	0.001 ± 0.001	0.008 ± 0.003	0.009 ± 0.007	0.002 ± 0.001	BDL	BDL
NO <sub>3</sub> <sup>-</sup>	0.01 ± 0.005	0.08 ± 0.02	0.18 ± 0.02	0.15 ± 0.02	0.03 ± 0.02	0.03 ± 0.01	0.06 ± 0.003
nss SO <sub>4</sub> <sup>=</sup>	0.004 ± 0.004	0.02 ± 0.01	0.02 ± 0.01	0.10 ± 0.05	0.03 ± 0.03	0.01 ± 0.002	0.02 ± 0.001
Sea salt	0.32 ± 0.01	0.20 ± 0.07	0.12 ± 0.03	0.16 ± 0.001	0.06 ± 0.004	0.06 ± 0.06	0.08 ± 0.004
H <sub>2</sub> O	0.63 ± 0.02	0.37 ± 0.16	0.19 ± 0.08	0.21 ± 0.06	0.14 ± 0.03	0.11 ± 0.09	0.15 ± 0.01
IOM (dust)	0.02 ± 0.02	0.22 ± 0.11	0.35 ± 0.05	0.21 ± 0.06	0.68 ± 0.09	0.76 ± 0.17	0.64 ± 0.03
POM	0.003 ± 0.005	0.08 ± 0.10	0.09 ± 0.06	0.12 ± 0.05	0.02 ± 0.03	0.02 ± 0.02	0.03 ± 0.001
EC	BDL	BDL	0.01 ± 0.01	0.01 ± 0.01	0.004 ± 0.004	0.003 ± 0.004	0.01 ± 0.004
				<i>Sub-10 μm</i>			
NH <sub>4</sub> <sup>+</sup>	0.01 ± 0.01	0.05 ± 0.02	0.05 ± 0.01	0.05 ± 0.01	0.02 ± 0.01	0.01 ± 0.01	0.02 ± 0.001
NO <sub>3</sub> <sup>-</sup>	0.01 ± 0.003	0.05 ± 0.001	0.10 ± 0.02	0.03 ± 0.01	0.03 ± 0.01	0.03 ± 0.01	0.05 ± 0.003
nss SO <sub>4</sub> <sup>=</sup>	0.04 ± 0.02	0.18 ± 0.10	0.15 ± 0.04	0.36 ± 0.06	0.10 ± 0.06	0.05 ± 0.02	0.08 ± 0.004
Sea salt	0.28 ± 0.03	0.12 ± 0.07	0.07 ± 0.03	0.04 ± 0.01	0.05 ± 0.01	0.05 ± 0.04	0.07 ± 0.003
H <sub>2</sub> O	0.57 ± 0.04	0.35 ± 0.10	0.23 ± 0.03	0.29 ± 0.06	0.17 ± 0.04	0.12 ± 0.08	0.18 ± 0.01
IOM (dust)	0.02 ± 0.02	0.12 ± 0.03	0.20 ± 0.05	0.06 ± 0.01	0.56 ± 0.15	0.67 ± 0.19	0.53 ± 0.03
POM	0.04 ± 0.02	0.11 ± 0.03	0.17 ± 0.05	0.14 ± 0.06	0.05 ± 0.04	0.06 ± 0.03	0.05 ± 0.002
EC	0.004 ± 0.002	0.01 ± 0.002	0.02 ± 0.01	0.01 ± 0.01	0.01 ± 0.01	0.01 ± 0.005	0.01 ± 0.001

<sup>a</sup>Standard deviations ( $1\sigma$ ) or uncertainty at the 95% confidence interval (for regions that have  $\leq 2$  samples) also are given. BDL, below detection limit.

Korea) suggests that nitrate preferentially reacted with the coarse mode dust and/or sea salt instead of the submicron ammonium and nss sulfate.

#### 4.3.3. Sub-10 $\mu\text{m}$ Aerosol

[71] Relatively low mean concentrations of sub- $10 \mu\text{m}$  aerosol were observed in the marine and polluted regions with higher concentrations in the dust regions (Figure 8). The sub- $10 \mu\text{m}$  mass fractions were composed primarily of sea salt and associated water in the Marine region, a mixture of sea salt, ammonium sulfate salts, dust and/or fly ash, and POM in the polluted regions, and primarily dust in the dust regions (Figure 9).

#### 4.4. Aerosol Size Distribution as a Function of Source Region

[72] Aerosol light scattering and hemispheric backscattering are determined, in large part, by the aerosol number size distribution. In addition, the measured size distribution was an integral part of the scattering calculations for both the total aerosol and the individual aerosol chemical components. Hence we show the surface area and volume size distributions derived from the measured number size distributions in Figure 10. An average distribution for each polluted and dust region is shown with variability indicated by  $1\sigma$  standard deviations of the average for each size bin. In addition, average submicron and supermicron surface area and volume concentrations and maximum modal diameters are listed in Table 5 for the different regions. Size distributions were not measured during the marine transit.

[73] Of the polluted regions, Volcano + Polluted had the largest accumulation mode (total submicron surface area of  $480 \pm 130 \mu\text{m}^2 \text{cm}^{-3}$ ) due to the mixture of both polluted and volcanic aerosol sources. It also had the smallest coarse mode (total supermicron surface area of  $16 \pm 2 \mu\text{m}^2 \text{cm}^{-3}$ ). The submicron surface area concentration for the Polluted – Korea/Japan and Polluted – Japan regions was 1.4 to 3 times lower ( $170 \pm 60$  and  $320 \pm 58 \mu\text{m}^2 \text{cm}^{-3}$ , respectively) while the supermicron concentrations were about a factor of 2 higher.

[74] Of the dust regions, Dust – Frontal had the largest accumulation and coarse modes with submicron and supermicron surface area concentrations of  $440 \pm 140$  and  $110 \pm 33 \mu\text{m}^2 \text{cm}^{-3}$ , respectively. The combination of appreciable accumulation and coarse modes was due to the mixing of polluted aerosol from the boundary layer with dust subsiding from aloft. Even though the magnitude of the accumulation and coarse modes varied within the three dust regions, they all had similar relative amounts of accumulation and coarse mode surface area.

#### 4.5. Aerosol Optical Properties as a Function of Source Region

##### 4.5.1. Aerosol Scattering and Hemispheric Backscattering Coefficients

[75] Percentile information for the sub- $10 \mu\text{m}$  aerosol light scattering coefficient measured at 550 nm and  $55 \pm 5\%$  RH is shown in Figure 11. To determine the relative contributions of the submicron and supermicron size

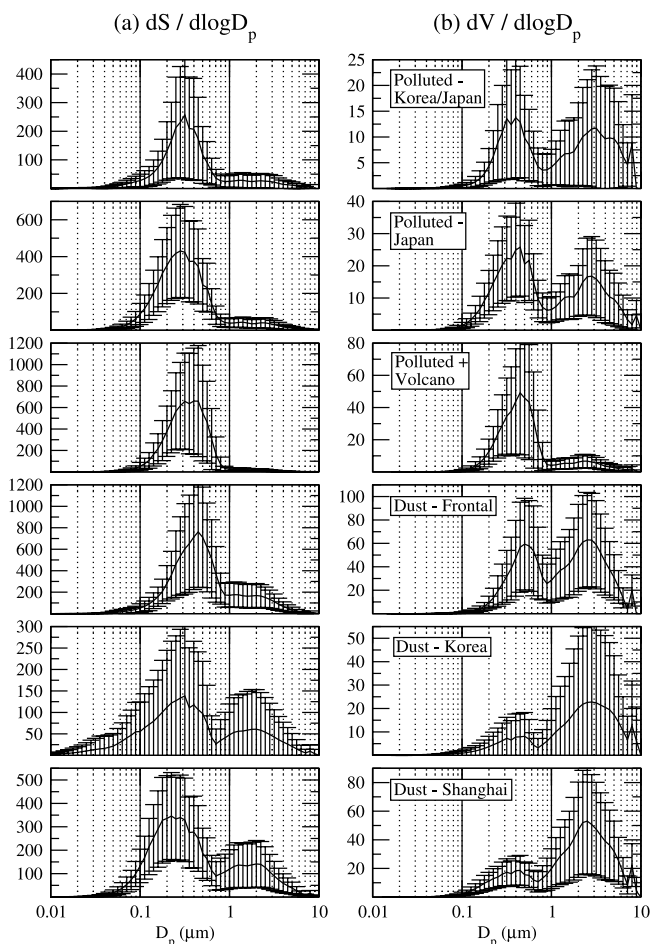


**Figure 10.** Average (a) surface area and (b) volume size distributions for the polluted and dust source regions. Error bars are  $1\sigma$  standard deviations of the average. Note changes in  $y$  axis scale between regions.

ranges to the scattering coefficient, the fine fraction of scattering,  $FF_{\text{scat}}$ , defined as

$$FF_{\text{scat}} = \sigma_{\text{sp}}(D_{\text{aero}} < 1.1\mu\text{m}) / \sigma_{\text{sp}}(D_{\text{aero}} < 10\mu\text{m}), \quad (6)$$

was calculated for each region (Figure 12). The lowest mean value of sub- $10\mu\text{m}$  light scattering was measured in the Marine region ( $29 \pm 17 \text{ Mm}^{-1}$ ) corresponding to low submicron and supermicron aerosol mass concentrations. On the basis of the sub- $10\mu\text{m}$  mass fractions and the  $FF_{\text{scat}}$ , supermicron sea salt clearly dominated both mass and

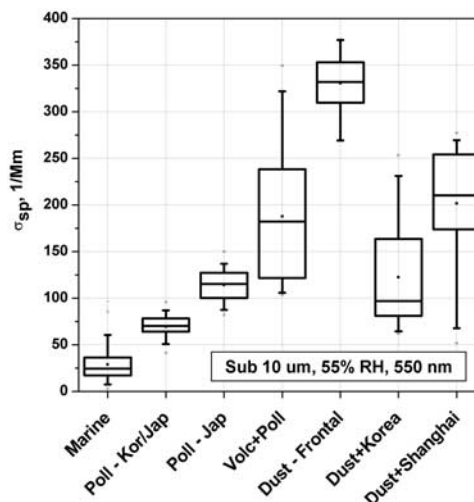


**Figure 11.** Sub- $10\mu\text{m}$  aerosol light scattering coefficient at  $550\text{ nm}$  and  $55\%$  RH for the seven regions. Percentile information is as in Figure 8.

scattering during the westward transit from Hawaii toward Japan.

[76] Sub- $10\mu\text{m}$  scattering coefficients were considerably higher in the polluted regions with mean values increasing from the Polluted – Korea/Japan region ( $69 \pm 11 \text{ Mm}^{-1}$ ) to the Polluted – Japan region ( $114 \pm 16 \text{ Mm}^{-1}$ ) to the Volcano + Polluted region ( $188 \pm 67 \text{ Mm}^{-1}$ ). Corresponding to this increase in sub- $10\mu\text{m}$  scattering were relatively large and increasing  $FF_{\text{scat}}$ . Mean values of  $FF_{\text{scat}}$  ranged from 0.69 to 0.87 showing the dominance of submicron aerosol (ammoniated sulfates and POM) in controlling the sub- $10\mu\text{m}$  scattering and the lesser importance of supermicron sea salt and dust. The Volcano + Polluted region had the highest mean  $FF_{\text{scat}}$  ( $0.87 \pm 0.06$ ). Acidic nss  $\text{SO}_4$  made the largest contribution to the submicron mass in this region ( $44 \pm 4\%$ ) presumably due to emissions from the Miyakejima volcano.

[77] Highest mean sub- $10\mu\text{m}$  scattering coefficients were measured in the dust regions with Dust – Frontal, Dust + Korea, and Dust + Shanghai having values of  $330 \pm 31$ ,  $120 \pm 57$ , and  $202 \pm 63 \text{ Mm}^{-1}$ , respectively. The  $FF_{\text{scat}}$  were low relative to the polluted regions due to the large concentrations of supermicron dust. The  $FF_{\text{scat}}$  are remarkably consistent for the three regions.

**Table 5.** Integral Submicron and Supermicron Particle Surface Area and Volume Concentrations (Mean and  $1\sigma$  Standard Deviation) at  $55\%$  RH for Each Region<sup>a</sup>

Region	Submicron				Supermicron			
	$S, \mu\text{m}^2 \text{ cm}^{-3}$	$D_{\text{gS}}, \mu\text{m}$	$V, \mu\text{m}^3 \text{ cm}^{-3}$	$D_{\text{gV}}, \mu\text{m}$	$S, \mu\text{m}^2 \text{ cm}^{-3}$	$D_{\text{gS}}, \mu\text{m}$	$V, \mu\text{m}^3 \text{ cm}^{-3}$	$D_{\text{gV}}, \mu\text{m}$
Polluted – Korea/Japan	$170 \pm 60$	0.32	$9 \pm 3.2$	0.40	$26 \pm 15$	1.4	$11 \pm 6.5$	2.5
Polluted – Japan	$340 \pm 67$	0.28	$17 \pm 3.3$	0.45	$33 \pm 12$	1.4	$13 \pm 5.5$	2.8
Volcano + Polluted	$490 \pm 120$	0.32	$29 \pm 10$	0.45	$16 \pm 2$	2.0	$6 \pm 0.62$	2.5
Dust – Frontal	$490 \pm 150$	0.45	$33 \pm 11$	0.50	$130 \pm 45$	2.0	$47 \pm 16$	2.5
Dust + Korea	$240 \pm 49$	0.32	$11 \pm 2.7$	0.50	$91 \pm 54$	2.0	$38 \pm 22$	2.8
Dust + Shanghai	$310 \pm 51$	0.22	$15 \pm 2.7$	0.45	$105 \pm 45$		$41 \pm 17$	2.5

<sup>a</sup>Surface area and volume maximum geometric diameters for the two size ranges also are given.

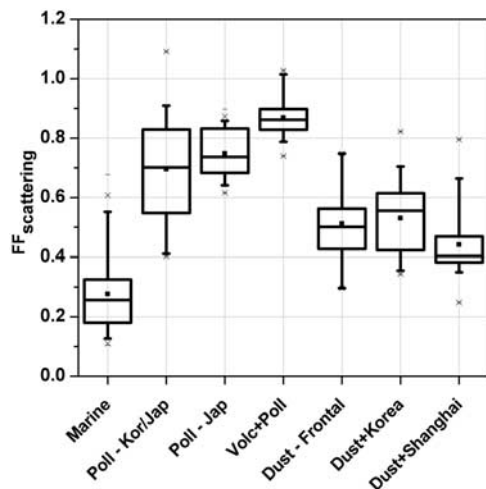


**Figure 12.** Ratio of the measured fine (sub-1  $\mu\text{m}$ ) to total (sub-10  $\mu\text{m}$ ) scattering coefficient at 550 nm and 55% RH. Percentile information is as in Figure 8.

[78] The Ångström exponent,  $\text{\AA}$ , for the sub-10  $\mu\text{m}$  aerosol and 550 and 700 nm wavelength pair was derived from

$$\text{\AA} = -\log(\sigma_{\text{sp},550}/\sigma_{\text{sp},700})/\log(550/700). \quad (7)$$

The Ångström exponent is a semiquantitative measure of the relative number of small- to large-sized particles contributing to the scattering such that smaller values of  $\text{\AA}$  indicate a larger average aerosol size and vice versa. Percentile information for  $\text{\AA}$  is shown in Figure 13. As expected, the trend in  $\text{\AA}$  was similar to that observed for  $\text{FF}_{\text{scat}}$ . In regions where the supermicron aerosol dominated the sub-10  $\mu\text{m}$  mass, surface area, and scattering,  $\text{\AA}$  was low (Marine =  $0.60 \pm 0.44$ , Dust – Frontal =  $0.92 \pm 0.39$ , Dust + Korea =  $0.70 \pm 0.38$ , and Dust + Shanghai =  $0.71 \pm 0.24$ ). In

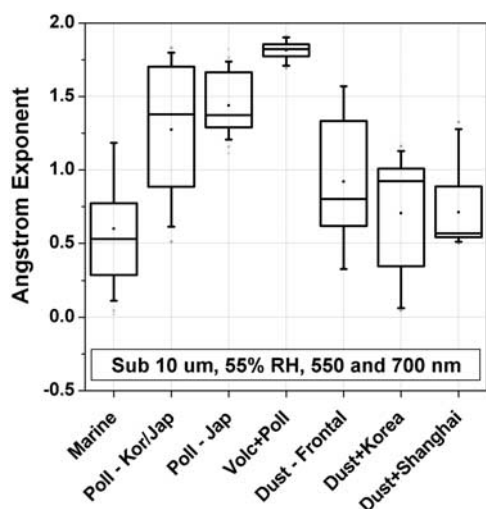


**Figure 13.** Ångström exponent for the 550 and 700 nm wavelength pair derived from the sub-10  $\mu\text{m}$  scattering coefficient measured at 550 nm and 55% RH. Percentile information is as in Figure 8.

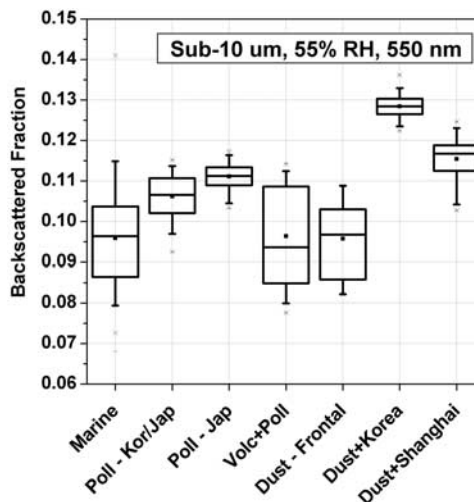


**Figure 14.** Backscattered fraction,  $b = \sigma_{\text{bsp}}/\sigma_{\text{sp}}$ , for the sub-10  $\mu\text{m}$  aerosol at 550 nm and  $55 \pm 5\%$  RH. Percentile information is as in Figure 8.

the polluted regions where the submicron aerosol dominated,  $\text{\AA}$  was relatively high (Polluted – Korea/Japan =  $1.3 \pm 0.43$ , Polluted – Japan =  $1.4 \pm 0.19$ , and Volcano + Polluted =  $1.8 \pm 0.05$ ).

[79] The hemispheric backscattered fraction,  $b$ , or the scattered intensity that is redirected into the backward hemisphere of the particle, was calculated from the ratio of the angular corrected backscattering coefficient ( $\sigma_{\text{bsp}, 90 \text{ to } 180^\circ}$ ) to the scattering coefficient ( $\sigma_{\text{sp}, 0 \text{ to } 180^\circ}$ ). Regional averages of  $b$  for the sub-10  $\mu\text{m}$  aerosol at 550 nm and  $55 \pm 5\%$  RH are shown in Figure 14. Mean values ranged from 0.096 to 0.11 for the marine and polluted regions. For the dust regions, mean  $\pm$  standard deviation values ranged from  $0.096 \pm 0.009$  for Dust – Frontal, to  $0.115 \pm 0.005$  for Dust + Shanghai, and  $0.128 \pm 0.003$  for Dust + Korea.

[80] Model calculations indicate that the scattering phase functions of sharp-edged irregular particles (i.e., dust-like) are larger than those of volume-equivalent spheres at forward scattering angles ( $< 10^\circ$ ) and smaller at backscattering angles ( $> 150^\circ$ ) [Kalashnikova and Sokolik, 2002]. Given this dependence of the scattering phase function on particle shape, smaller  $b$  values for the dust regions relative to the polluted regions would be predicted. The opposite was observed for the Dust + Korea and Dust + Shanghai cases. It is most likely that the observed trends in  $b$  values were due to the competing effects of particle shape and size. For particle diameters greater than about 1  $\mu\text{m}$  (geometric),  $b$  increases with increasing size. Higher values of  $b$  for the sub-10  $\mu\text{m}$  aerosol corresponded to regions with a particle population dominated by larger particles.

#### 4.5.2. Aerosol Absorption Coefficient and Single Scattering Albedo

[81] Percentile information for the sub-10  $\mu\text{m}$  aerosol absorption coefficient at 550 nm and  $55 \pm 5\%$  RH is shown in Figure 15. As for the sub-10  $\mu\text{m}$  scattering coefficient, the lowest mean value was observed in the marine region ( $0.79 \pm 0.71 \text{ Mm}^{-1}$ ). Values in the polluted regions averaged  $7.9 \pm 1.5 \text{ Mm}^{-1}$  for Polluted – Korea/Japan,  $11 \pm 2.1 \text{ Mm}^{-1}$  for Polluted – Japan, and  $9.0 \pm 3.0 \text{ Mm}^{-1}$  for

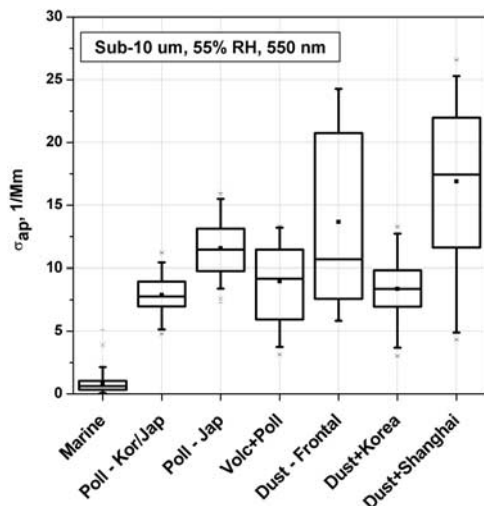


**Figure 15.** Sub-10  $\mu\text{m}$  aerosol light absorption coefficient at 550 nm and 55% RH for the seven regions. Percentile information is as in Figure 8.

Volcano + Polluted. The mean absorption coefficient for the Dust + Korea region ( $8.4 \pm 2.5 \text{ Mm}^{-1}$ ) was similar to the polluted regions. In the Dust – Frontal and Dust + Shanghai regions, however, mean values were higher ( $14 \pm 7.0$  and  $17 \pm 6.5 \text{ Mm}^{-1}$ , respectively) and the range of values was greater. The sub-10  $\mu\text{m}$  EC mass fractions for all regions were around 1–2%.

[82] Clear differences between the polluted and dust regions are seen in the fine fraction of absorption,  $\text{FF}_{\text{absorp}}$  (Figure 16). In the polluted regions, mean values of  $\text{FF}_{\text{absorp}}$  fell within the range of 88 to 93%. In the dust regions mean values ranged between 73 and 77% indicating that a larger portion of the EC was associated with supermicron particles.  $\text{FF}_{\text{absorp}}$  in the marine region was noisy due to levels of absorption being near the detection limit of the PSAP. On the basis of secondary electron images of individual particles collected on the ship (Figure 17), the supermicron

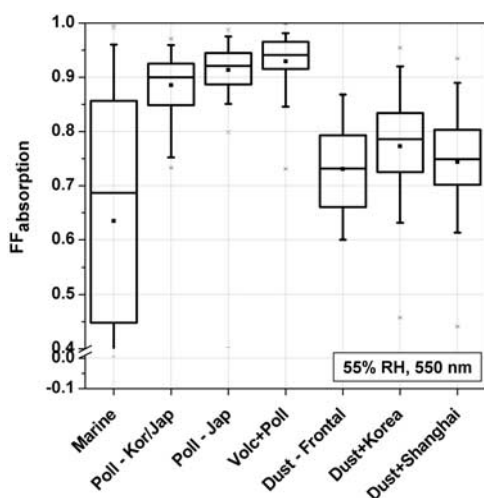


**Figure 16.** Ratio of the fine (submicron) to total (sub-10  $\mu\text{m}$ ) aerosol light absorption coefficients at  $55 \pm 5\%$  RH and 550 nm. Percentile information is as in Figure 8.

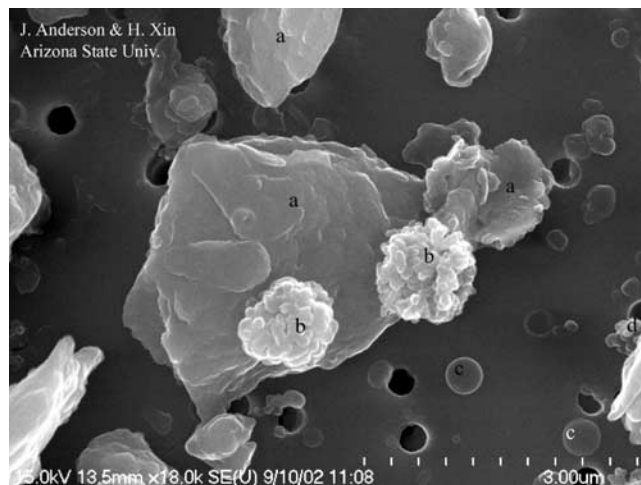


**Figure 17.** Secondary electron image of an aggregate particle consisting of (a) silicate dust and (b) soot. The primary spherule size in soot (b) is 100–150 nm. Separate black (c) carbon spheres and (d) other soot types with smaller primary spherules are also present in the field of view. This 2 hour sample was collected on DOY 102 (12 April) during the Dust + Korea period, when the ship was in the southern Sea of Japan. The full length of the scale bar is 3.0  $\mu\text{m}$ . This was imaged with an Hitachi S4700 Cold Field Emission Scanning Electron Microscope.

absorption in the dust regions was a result of the presence of several types of supermicron soot including dust-soot aggregates and solitary black carbon cenospheres. Dust-soot aggregates also were observed in samples collected on the NCAR C-130. Implications of the supermicron soot and absorption are discussed in more detail below.

[83] Single scattering albedo, defined as

$$\omega = \sigma_{\text{sp}} / (\sigma_{\text{sp}} + \sigma_{\text{ap}}), \quad (8)$$

is a relative measure of the scattering and extinction coefficients of the aerosol with lower values indicating a more absorbing aerosol. It is a key parameter in models used to calculate aerosol radiative forcing and in algorithms used to retrieve aerosol properties from satellites. Using the measured scattering coefficient (corrected for angular nonidealities) and measured absorption coefficient (corrected as per Bond *et al.* [1999]),  $\omega$  was calculated for the sub-10  $\mu\text{m}$  aerosol at  $55 \pm 5\%$  RH and STP. For all regions, mean values of  $\omega$  were greater than or equal to 0.9 (Figure 18). For the polluted regions, mean values ranged from 0.9 to 0.94 and for the dust regions from 0.92 to 0.96. The lowest values were measured in the Polluted – Korea/ Japan region where the 25th percentile was 0.89. For comparison, the mean 55% RH value observed for the east Indian subcontinent source region during INDOEX was  $0.86 \pm 0.01$  [Quinn *et al.*, 2002].

[84] Single scattering albedo also was calculated at ambient RH by adjusting the scattering coefficient measured at 55% RH to ambient RH using values of  $f(\text{RH})$  measured on board RHB [Carrico *et al.*, 2003]. These values of  $\omega$  at ambient RH assume that  $f(\text{RH})$  for absorption is equal to one. Figure 18 shows  $\omega$  calculated at ambient RH along

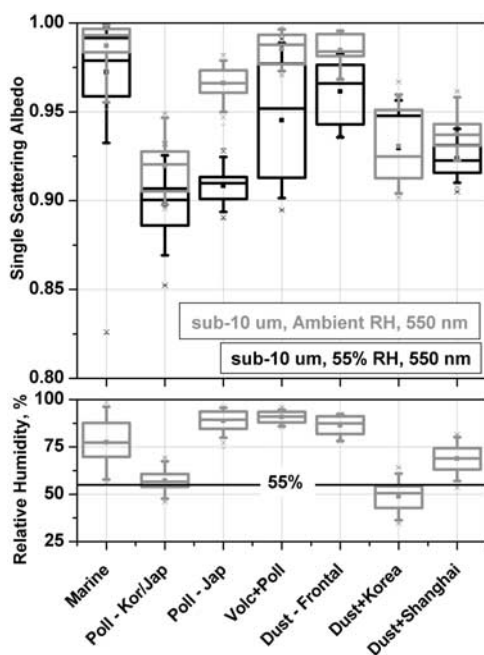


**Figure 18.** Single scattering albedo for sub-10  $\mu\text{m}$  aerosol at 55% and ambient RH. Values are shown for the seven source regions. Ambient RH for the source regions also is shown. Percentile information is as in Figure 8. See color version of this figure in the HTML.

with ambient RH values for each region. In the marine region,  $\omega$  at 55% and ambient RH were very similar (mean values of  $0.97 \pm 0.03$  and  $0.99 \pm 0.01$ , respectively) since the aerosol was composed primarily of aerosol components that scatter and don't absorb at visible wavelengths. As expected, single scattering albedo at 55% and ambient RH also were similar in regions where the ambient RH was close to 55% (Polluted – Korea/Japan, Dust + Korea, and Dust + Shanghai). The largest difference between the two quantities was found in the Polluted – Japan region. The mean value at 55% RH was  $0.91 \pm 0.01$ . At ambient RH ( $89 \pm 5.4\%$ ), the mean value was  $0.97 \pm 0.01$ . In contrast, ambient RH also was high in the Dust – Frontal region ( $86 \pm 4.6\%$ ) but the 55% and ambient RH  $\omega$  were similar ( $0.96 \pm 0.02$  and  $0.98 \pm 0.01$ , respectively). Presumably the dust, which made up almost 60% of the sub-10  $\mu\text{m}$  aerosol mass in the Dust – Frontal region made for a less hygroscopic aerosol than the pollution aerosol of the Polluted – Japan region.

[85] As stated above, the values of  $\omega$  presented here at ambient RH do not take into account any change in the absorption coefficient due to changes in ambient RH. Hence it is not strictly an “ambient RH”  $\omega$ . The comparison of this quantity to that measured at 55% RH does, however, indicate the sensitivity of  $\omega$  to RH, the dependence of this sensitivity on aerosol chemical composition, and the importance of stating the RH at which  $\omega$  is reported.

#### 4.5.3. Optical Effects of Supermicron Dust–Soot Dust Aggregates

[86] As shown in Figure 17, scanning electron microscopy (SEM) analysis of single particles collected during ACE-Asia show direct evidence for supermicron dust-soot aggregates. This sample, collected on DOY 102 during the Dust + Korea

period, contains silicate dust (a) aggregated with soot having a primary spherule size of 100 to 150 nm (b). Also present in the image are soot types with smaller primary spherules (d) and solitary black carbon cenospheres (c). Carbon cenospheres are hollow balls of black carbon formed by pyrolysis during combustion of heavy fuel oil or coal. They are very stable under the high electron beam current used in the SEM analysis with the only detectable element being C. Other samples revealed carbon cenospheres as large as 5  $\mu\text{m}$  in diameter. The optical properties of the soot are expected to vary with morphology (aggregated spherules vs. solitary sphere), diameter of the spherules or solitary spheres, structure of the aggregated spherules, and character of association with other particle types (e.g., mixing state) [e.g., Fuller *et al.*, 1999]. Modeling the sensitivity of the particle optical properties to these differences is outside of the scope of this paper. However, we can consider the impact of the supermicron black carbon on the measured aerosol chemical and optical properties.

[87] Supermicron EC was detected in five of the seven regions with mean concentrations in the dust regions of  $0.38 \pm 0.09 \mu\text{g C m}^{-3}$  (Dust – Frontal),  $0.15 \pm 0.15 \mu\text{g C m}^{-3}$  (Dust + Korea), and  $0.86 \pm 0.21 \mu\text{g C m}^{-3}$  (Dust + Shanghai) (Figure 19a). Detectable supermicron absorption was measured in all regions but was highest in the three Dust regions with mean values of  $3.8 \pm 2.3 \text{ Mm}^{-1}$  (Dust – Frontal),  $2.1 \pm 1.1 \text{ Mm}^{-1}$  (Dust + Korea), and  $4.6 \pm 2.7 \text{ Mm}^{-1}$  (Dust + Shanghai) (Figure 19c). As discussed above, mean values of the  $\text{FF}_{\text{absorb}}$  ranged from 88 to 93% outside of the dust regions and from 73 to 77% in the dust regions (Figure 16). The supermicron absorption was overwhelmed by the supermicron scattering in the dust regions, however (Figure 19b), resulting in relatively high values of  $\omega$ . The mean ambient RH supermicron  $\omega$  for the dust regions ranged between 0.97 and 0.99 (Figure 19d). Hence the supermicron soot appears to have had a negligible effect on the supermicron single scattering albedo. The larger implication for the soot-dust aggregates is the shortening of the lifetime of soot due to its association with supermicron particles and the removal of soot from the submicron size range to the less optically efficient supermicron size range.

#### 4.6. Regional Scattering Due to Individual Aerosol Chemical Components

[88] The fraction of the measured scattering due to the dominant aerosol chemical components was calculated at 55% RH and a wavelength of 550 nm using the method described in section 3. The components considered are sea-salt aerosol which includes supermicron  $\text{NO}_3^-$  and water calculated to be associated with sea salt at 55% RH; nss sulfate aerosol which includes nss  $\text{SO}_4^{2-}$ ,  $\text{NH}_4^+$ , and water at 55% RH; POM; EC; and IOM (Dust). Results are shown in Figure 20 for the submicron, supermicron, and sub-10  $\mu\text{m}$  aerosol. The regional average and standard deviation ( $1\sigma$ ) of the scattering fractions are given in Table 6 for the three size ranges. Scattering fractions were not calculated for the Marine region as no size distributions were available.

##### 4.6.1. Submicron Aerosol

[89] In general, for all size ranges, the trend in scattering fractions for the dominant chemical components followed the trend in mass fractions. Submicron scattering was controlled primarily by nss sulfate aerosol, sea salt, and

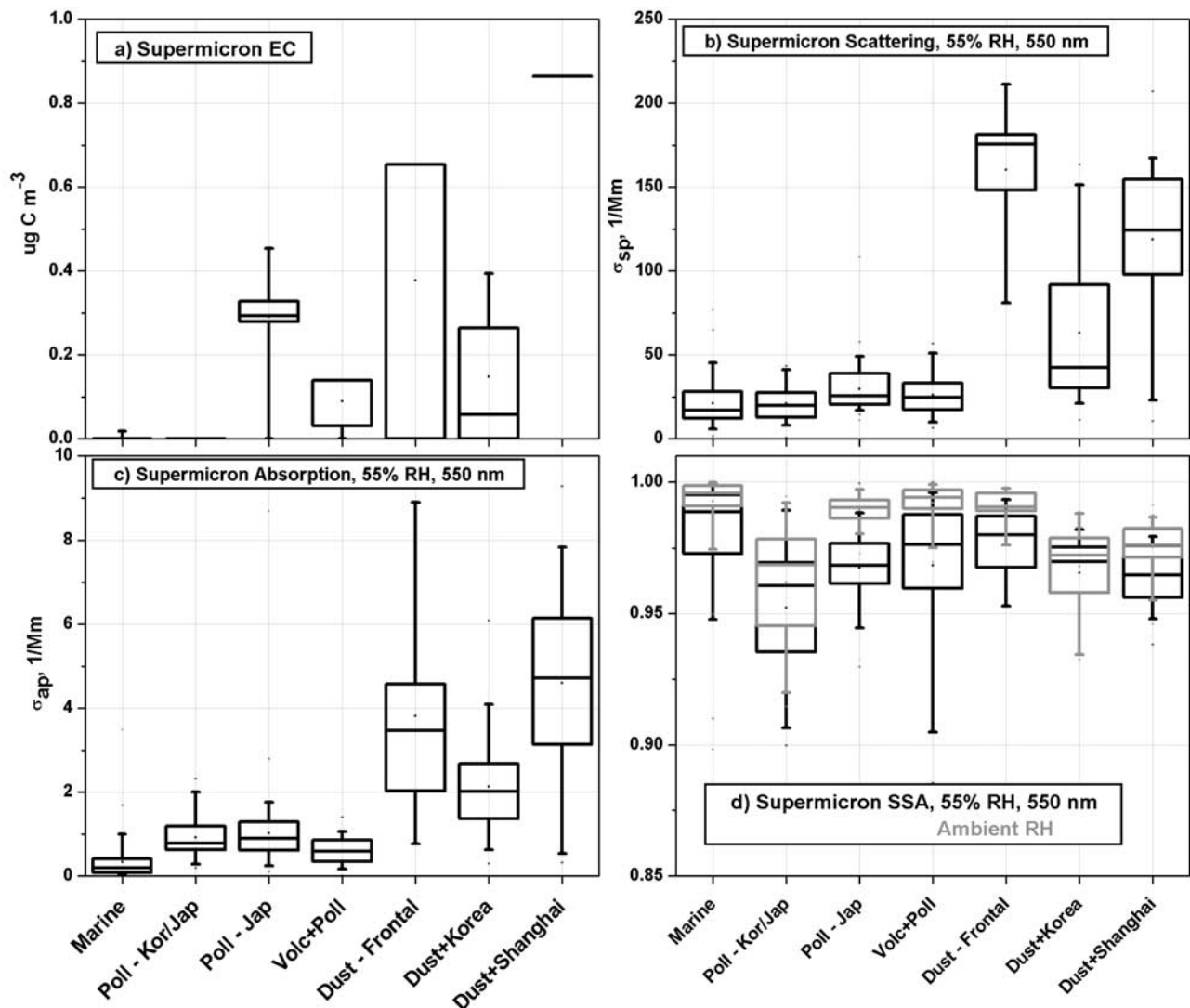


**Figure 19.** Shown for the seven regions are supermicron (a) EC, (b) scattering coefficient, (c) absorption coefficient, and (d) single scattering albedo at 55% and ambient RH. Percentile information is as in Figure 8. See color version of this figure in the HTML.

POM in the Polluted – Korea/Japan, Polluted – Japan, and Volcano + Polluted regions. Non-sea-salt sulfate dominated in all three of these regions and had the largest contribution in the Volcano + Polluted region due to a combination of pollution and volcanic sources. IOM (Dust) had a significant contribution to the submicron scattering in the Dust regions and dominated in the Dust + Korea region. Over all regions, the contribution to submicron scattering due to sea salt ranged from 9 to 33%. This nonnegligible contribution in spite of relatively low mass fractions is a result of the propensity of sea salt to absorb water with increasing RH and its reluctance to release the water with decreasing RH. As RH decreases from 70 to 55%, sea salt retains water such that the wet particle mass is twice its dry mass [Tang *et al.*, 1997]. Mean regional submicron scattering fractions of elemental carbon ranged from 2 to 4% corresponding to its low mass fractions.

#### 4.6.2. Supermicron and Sub-10 $\mu\text{m}$ Aerosol

[90] The supermicron size range showed a decreased contribution of nss sulfate aerosol and an increased contri-

bution of nitrate, sea salt, and dust to scattering by the aerosol when compared to the submicron aerosol. In the Polluted – Korea/Japan, Polluted – Japan, and Volcano + Polluted regions, sea salt dominated but was accompanied by significant contributions of POM. In the three dust regions, dust overwhelmed the contributions by all other components.

[91] The sub-10  $\mu\text{m}$  aerosol indicates two regimes. One includes the three polluted regions where POM, nss sulfate, and sea salt all have significant contributions to the scattering. The other includes the three dust regions where these same components contribute to scattering but dust dominates.

### 4.7. Mass Scattering Efficiencies of the Individual Aerosol Chemical Components

#### 4.7.1. Comparison of Two Methods

[92] Mass scattering efficiencies of the individual chemical components,  $\alpha_{sp,j}$ , are defined as

$$\alpha_{sp,j} = \frac{\sigma_{sp,j}}{m_j}, \quad (9)$$

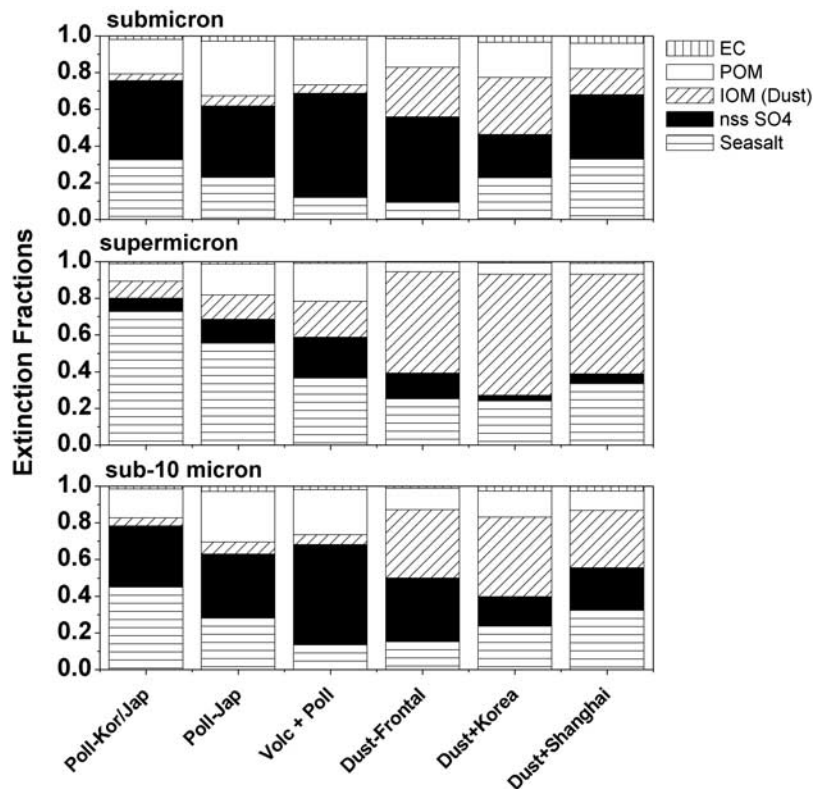


**Figure 20.** Mean regional fractional contribution of the dominant aerosol chemical components to scattering. Scattering fractions are reported at 55% RH and 550 nm for the (top) submicron, (middle) supermicron, and (bottom) sub-10  $\mu\text{m}$  size ranges. See color version of this figure in the HTML.

where  $\sigma_{\text{sp},j}$  is the scattering coefficient for component  $j$  and  $m_j$  is the mass of component  $j$ . An empirical and a calculational approach were used to calculate  $\alpha_{\text{sp},j}$  for the sub-10  $\mu\text{m}$  size range to check for consistency between the methods. The empirical approach used a multiple linear regression of the mass concentration of the dominant chemical components against the measured scattering coefficient. The following equation was used to derive weighted averages of the component mass scattering efficiencies:

$$\sigma_{\text{sp}} = \alpha_{\text{sp,seasalt}}m_{\text{seasalt}} + \alpha_{\text{sp,nssSulfate}}m_{\text{nssSulfate}} + \alpha_{\text{sp,IOM}}m_{\text{IOM}} + \alpha_{\text{sp,POM}}m_{\text{POM}}, \quad (10)$$

where  $\sigma_{\text{sp}}$  is the measured light scattering coefficient and the mass concentrations are a sum of the measured submicron and supermicron concentrations for each component. Rather than deriving regional values, the entire data set was used (exclusive of the Marine region) because of the small number of samples collected in some regions. The calculational approach was based on the Mie calculations described in section 3.

[93] Mean values from the two approaches are compared in Table 7. For all components,  $\sigma_{\text{sp},j}$  calculated from the multiple linear regression lies within the range of values derived from the Mie calculations. The agreement between the two independent methods confirms the internal consistency in the data set and indicates that the derived compo-

nent mass scattering efficiencies are accurate within experimental uncertainty.

#### 4.7.2. Submicron, Supermicron, and Sub-10 $\mu\text{m}$ Component Mass Scattering Efficiencies

[94] The calculational method also was used to derive  $\alpha_{\text{sp},j}$  for the submicron, supermicron, and sub-10  $\mu\text{m}$  size ranges for the different regions (see Table 8). Mean mass scattering efficiencies of submicron sea salt ranged from 4.5 to 5.8  $\text{m}^2 \text{g}^{-1}$ . Supermicron values ranged from 1.3 to 1.9  $\text{m}^2 \text{g}^{-1}$ . These values compare well with those estimated for the central Pacific (3.5 to 7.7  $\text{m}^2 \text{g}^{-1}$  and 0.39 to 1.1  $\text{m}^2 \text{g}^{-1}$  for the submicron and supermicron size ranges, respectively) [Quinn *et al.*, 1996], the Atlantic (5.2 to 6.9  $\text{m}^2 \text{g}^{-1}$  and 0.9 to 1.3  $\text{m}^2 \text{g}^{-1}$  for the submicron and supermicron size ranges, respectively) [Quinn *et al.*, 2001], and the northern Indian Ocean (5.1 to 6.0  $\text{m}^2 \text{g}^{-1}$  and 1.0 to 1.2  $\text{m}^2 \text{g}^{-1}$  for the submicron and supermicron size ranges, respectively) [Quinn *et al.*, 2002].

[95] Mean  $\alpha_{\text{sp},j}$  for submicron nss  $\text{SO}_4^-$  aerosol ranged from 3.0 to 4.7  $\text{m}^2 \text{g}^{-1}$ . These values also are comparable to those previously reported for the central Pacific (4.3 to 7.5  $\text{m}^2 \text{g}^{-1}$ ) [Quinn *et al.*, 1996], Atlantic (2.6 to 4.3  $\text{m}^2 \text{g}^{-1}$ ) [Quinn *et al.*, 2001], and northern Indian Ocean (2.9 to 5.3  $\text{m}^2 \text{g}^{-1}$ ) [Quinn *et al.*, 2002]. In addition, they fall within the range of low RH sulfate scattering efficiencies predicted by Charlson *et al.* [1999]. Mean  $\alpha_{\text{sp},j}$  for submicron IOM (Dust) ranged from 3.0 to 3.9  $\text{m}^2 \text{g}^{-1}$  and for the supermicron size range from 0.43 to 0.82  $\text{m}^2 \text{g}^{-1}$ . These values are similar for African dust that had been transported to the central Atlantic ( $3.5 \pm 0.6 \text{ m}^2 \text{g}^{-1}$  and  $0.5 \pm 0.1 \text{ m}^2 \text{g}^{-1}$  for

**Table 6.** Average and Standard Deviation ( $1\sigma$ ) of the Regional Scattering Fractions of the Dominant Aerosol Chemical Components for the Submicron ( $D_{\text{aero}} < 1.1 \mu\text{m}$ ), Supermicron ( $1.1 < D_{\text{aero}} < 10 \mu\text{m}$ ), and Sub- $10 \mu\text{m}$  ( $D_{\text{aero}} < 10 \mu\text{m}$ ) Size Ranges

Component	Polluted – Korea/Japan	Polluted/Japan	Volcano + Polluted	Dust – Frontal	Dust + Korea	Dust + Shanghai
<i>Submicron</i>						
Sea salt	0.33 ± 0.04	0.23 ± 0.02	0.12 ± 0.04	0.09 ± 0.01	0.23 ± 0.14	0.33 ± 0.10
nss SO <sub>4</sub> <sup>−</sup> aerosol	0.43 ± 0.62	0.39 ± 0.05	0.57 ± 0.04	0.46 ± 0.03	0.23 ± 0.09	0.35 ± 0.07
POM	0.19 ± 0.27	0.30 ± 0.04	0.25 ± 0.04	0.15 ± 0.02	0.19 ± 0.05	0.14 ± 0.01
EC	0.02 ± 0.03	0.03 ± 0.007	0.02 ± 0.004	0.02 ± 0.001	0.03 ± 0.009	0.04 ± 0.006
IOM (dust)	0.03 ± 0.05	0.05 ± 0.009	0.04 ± 0.004	0.27 ± 0.07	0.31 ± 0.06	0.14 ± 0.02
<i>Supermicron</i>						
Sea salt	0.73 ± 0.99	0.56 ± 0.09	0.37 ± 0.05	0.25 ± 0.02	0.24 ± 0.11	0.34 ± 0.007
nss SO <sub>4</sub> <sup>−</sup> aerosol	0.07 ± 0.11	0.13 ± 0.04	0.22 ± 0.02	0.14 ± 0.02	0.03 ± 0.02	0.05 ± 0.02
POM	0.10 ± 0.15	0.17 ± 0.06	0.21 ± 0.07	0.05 ± 0.02	0.06 ± 0.04	0.06 ± 0.01
EC	0.01 ± 0.01	0.01 ± 0.003	0.01 ± 0.003	0.003 ± 0.001	0.008 ± 0.002	0.009 ± 0.001
IOM (dust)	0.09 ± 0.12	0.13 ± 0.03	0.20 ± 0.03	0.55 ± 0.06	0.66 ± 0.06	0.54 ± 0.04
<i>Sub-10 μm</i>						
Sea salt	0.45 ± 0.56	0.28 ± 0.04	0.14 ± 0.04	0.15 ± 0.02	0.24 ± 0.14	0.32 ± 0.06
nss SO <sub>4</sub> <sup>−</sup> aerosol	0.33 ± 0.43	0.35 ± 0.05	0.54 ± 0.04	0.35 ± 0.07	0.16 ± 0.07	0.23 ± 0.08
POM	0.16 ± 0.19	0.28 ± 0.05	0.24 ± 0.04	0.12 ± 0.03	0.14 ± 0.05	0.11 ± 0.02
EC	0.02 ± 0.02	0.03 ± 0.006	0.02 ± 0.003	0.01 ± 0.003	0.03 ± 0.008	0.03 ± 0.002
IOM (dust)						

the submicron and supermicron size ranges, respectively) [Quinn *et al.*, 2001] and to dust from the Indian subcontinent ( $3.3 \pm 0.7 \text{ m}^2 \text{ g}^{-1}$  and  $0.6 \pm 0.1 \text{ m}^2 \text{ g}^{-1}$ , respectively) [Quinn *et al.*, 2002].

[96] Submicron mean  $\alpha_{\text{sp},j}$  for POM ranged from 4.4 to  $6.0 \text{ m}^2 \text{ g}^{-1}$  and agreed with values estimated for Atlantic and northern Indian Ocean aerosol ( $5.0$  to  $7.5 \text{ m}^2 \text{ g}^{-1}$  and  $5.4$  to  $7.6 \text{ m}^2 \text{ g}^{-1}$ , respectively) [Quinn *et al.*, 2001, 2002]. Supermicron values ranged from 1.7 to  $2.4 \text{ m}^2 \text{ g}^{-1}$  which are comparable to the Atlantic range of values of 1.1 to  $2.1 \text{ m}^2 \text{ g}^{-1}$  but considerably lower than those determined for the northern Indian Ocean ( $2.8$  to  $5.5 \text{ m}^2 \text{ g}^{-1}$ ). The higher Indian Ocean values could be a result of a different organic composition, size distribution, and/or sampling and analysis methods. Submicron and supermicron mean  $\alpha_{\text{sp},j}$  for the EC aerosol component ranged from 3.8 to 4.0 and  $0.51$  to  $0.89 \text{ m}^2 \text{ g}^{-1}$ , respectively.

#### 4.8. Aerosol Optical Depth and Vertical Profiles

[97] Regional averages and  $1\sigma$  standard deviations of aerosol optical depth,  $\tau_a$ , are shown in Figure 21. Also shown are surface extinction coefficients,  $\sigma_{\text{ep}}$ , derived from measured values of  $\sigma_{\text{sp}}$  and  $\sigma_{\text{ap}}$ . As for surface  $\sigma_{\text{ep}}$ , values of  $\tau_a$  were low in the Marine region ( $0.17 \pm 0.07$ ) and increased through the three polluted regions. Average values

**Table 7.** Comparison of Mass Scattering Efficiencies Derived From Mie Calculations (Calculated) and From a Multiple Linear Regression (Empirical) at  $550 \text{ nm}^a$ 

Component	Empirical <sup>b</sup>		Calculated	
	Coefficient	Standard Error	Mean	Range
Sea-salt aerosol	1.4	0.26	2.8	1.4–4.4
nss SO <sub>4</sub> <sup>−</sup> aerosol	4.4	0.25	3.6	2.6–4.8
IOM (dust)	1.1	0.08	1.3	0.53–4.1
POM	4.2	1.1	4.4	2.9–6.0

<sup>a</sup>Values are for the size range  $D_{\text{aero}} < 10 \mu\text{m}$  (at 55% RH) and are means over the entire experiment. Units are in  $\text{m}^2 \text{ g}^{-1}$ .

<sup>b</sup>On the basis of equation (8);  $r^2 = 0.96$ ; number of samples equal to 54.

during Polluted – Korea/Japan, Polluted – Japan, and Volcano + Polluted were  $0.38 \pm 0.04$ ,  $0.42 \pm 0.10$ , and  $0.82 \pm 0.19$ , respectively. Clouds prevented measurements of  $\tau_a$  during the Dust – Frontal period.  $\tau_a$  was similar during Dust + Korea and Dust + Shanghai averaging  $0.39 \pm 0.12$  and  $0.31 \pm 0.05$ , respectively.

[98] Differences in the surface and column-integrated aerosol size distributions can be inferred from Ångström exponents derived from surface scattering coefficients versus those derived from  $\tau_a$ . Ångström exponents were calculated for the surface and column aerosol from the nephelometer and Sun photometer/radiometer measurements, respectively. A linear fit of  $\ln(\text{wavelength})$  versus  $\ln(\sigma_{\text{sp}}$  or  $\tau_a)$  values for three wavelengths in the 400 to 700 nm region were used (section 2.6). A comparison of regional averages for the surface and atmospheric column are shown in Figure 22.

[99] The surface and column  $\text{Å}$  values agreed within 6% for the Marine region. On DOY 81, when the lidar measurements for this region were made, there was a well mixed boundary layer with a height of about 0.75 km (Figure 23). Here, the top of the marine boundary layer is defined by the beginning of a strong negative gradient in RH and/or a temperature inversion. On the basis of a total column height of 7 km,  $60 \pm 150\%$  of the column extinction was due to aerosol in the marine boundary layer. The relatively low and uniform  $\text{Å}$  through the atmospheric column coupled with the large sub- $10 \mu\text{m}$  mass fraction of sea-salt aerosol, indicates that sea salt controlled both the surface and column optical properties in this region. It is possible, however, that upper altitude dust also contributed to the relatively low column derived  $\text{Å}$  value. The lidar measurements indicated the presence of weak aerosol layers between 2 and 6 km and the 2500 m trajectories suggested upper level flow from the N. China and Mongolia dust regions.

[100] In the Polluted – Korea/Japan region, the average surface  $\text{Å}$  was  $33 \pm 36\%$  higher than the column  $\text{Å}$ . The vertical profiles of RH and temperature in this region showed a well-mixed boundary layer with a height of about

**Table 8.** Mean and Standard Deviation ( $1\sigma$ ) of the Regional Mass Scattering Efficiencies of the Dominant Aerosol Chemical Components<sup>a</sup>

Region	Sea Salt <sup>b</sup>		nss SO <sub>4</sub> <sup>c</sup> Aerosol <sup>e</sup>		IOM (Dust)		POM		EC and nss K <sup>+</sup> <sup>d</sup>		Total Aerosol	
	Mean	SD	Mean	SD	Mean	SD	Mean	SD	Mean	SD	Mean	SD
	<i>Submicron, m<sup>2</sup>g<sup>-1</sup></i>											
Polluted – Korea/Japan	4.6	0.68	3.9	0.42	3.0	0.32	5.5	0.33	3.9	0.21	4.3	0.17
Polluted – Japan	4.6	0.50	3.5	0.08	3.4	0.21	5.3	0.20	3.9	0.12	4.1	0.09
Volcano + Polluted	4.5	0.58	4.3	0.31	3.3	0.41	5.9	0.22	3.8	0.08	5.1	0.34
Dust + Frontal	5.1	1.0	4.7	0.18	3.9	0.09	6.0	0.24	4.0	0.32	4.8	0.29
Dust + Korea	5.2	1.5	3.0	0.27	3.4	0.26	4.5	0.24	3.9	0.20	3.8	0.27
Dust + Shanghai	5.8	1.2	3.2	0.19	3.1	0.24	4.4	0.37	3.8	0.15	3.6	0.23
	<i>Supermicron, m<sup>2</sup>g<sup>-1</sup></i>											
Polluted – Korea/Japan	1.3	0.15	2.8	0.62	0.43	0.04	2.0	0.77	0.57	0.06	1.0	0.07
Polluted – Japan	1.5	0.31	2.8	0.71	0.51	0.05	1.7	0.11	0.51	0.06	1.0	0.07
Volcano + Polluted	1.4	0.18	2.8	0.36	0.82	0.13	1.8	0.26	0.53	0.09	2.6	0.96
Dust + Frontal	1.7	0.05	3.4	0.23	0.82	0.11	2.4	0.63	0.89	0.42	1.4	0.32
Dust + Korea	1.5	0.09	3.8	0.78	0.72	0.04	2.1	0.76	0.61	0.20	1.1	0.08
Dust + Shanghai	1.9	0.12	3.5	0.29	0.70	0.04	1.9	0.11	0.54	0.03	1.1	0.11
	<i>Sub-10 μm, m<sup>2</sup>g<sup>-1</sup></i>											
Polluted – Korea/Japan	2.3	0.43	3.8	0.25	0.89	0.31	4.4	1.0	2.0	0.47	2.3	0.47
Poll – Japan	2.8	0.34	3.3	0.10	1.3	0.31	4.5	0.25	2.7	0.40	2.8	0.36
Volcano + Polluted	3.3	0.63	4.2	0.32	1.9	0.19	5.2	0.44	3.1	0.28	4.3	0.63
Dust + Frontal	2.4	0.51	4.5	0.16	1.3	0.42	4.8	0.53	2.9	0.59	2.4	0.76
Dust + Korea	2.8	0.63	3.0	0.29	1.1	0.79	3.8	0.83	2.5	0.57	1.8	1.0
Dust + Shanghai	3.1	0.36	3.2	0.16	0.94	0.25	3.4	0.36	2.1	0.31	1.6	0.37

<sup>a</sup>Integral values are reported at 55% RH for the submicron ( $D_{\text{aero}} < 1.1 \mu\text{m}$ ), supermicron ( $1.1 < D_{\text{aero}} < 10 \mu\text{m}$ ), and sub-10  $\mu\text{m}$  size ranges. Values were calculated using the method described in section 3.

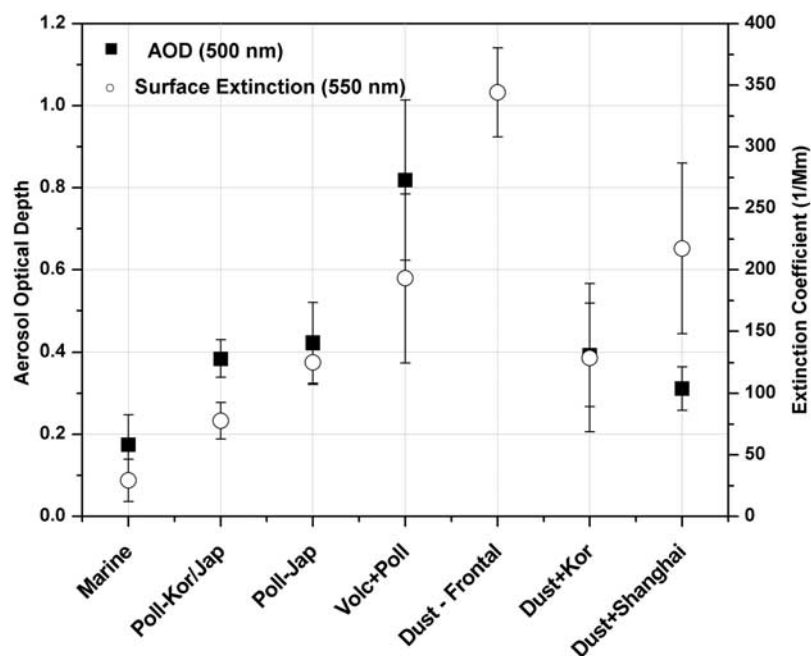
<sup>b</sup>Includes NO<sub>3</sub><sup>-</sup> and water at 55% RH.

<sup>c</sup>Includes nss SO<sub>4</sub><sup>-</sup>, NH<sub>4</sub><sup>+</sup>, and water at 55% RH.

<sup>d</sup>nss K<sup>+</sup> with associated SO<sub>4</sub><sup>-</sup> and NO<sub>3</sub><sup>-</sup>.

1.5 km (Figure 23). The aerosol extinction profile was similar with the top of the lowest aerosol layer at about 1.5 km. A second but weaker aerosol layer (based on lower extinction values) was present around 2 km. On the basis of a total column height of 7 km,  $73 \pm 4.6\%$  of the column

extinction was due to aerosol in the boundary layer. The 5500 m trajectory corresponding to the lidar measurement suggested flow from the Gobi desert. Hence the aerosol extinction in the upper troposphere may have been due to dust. The presence of dust layers aloft would help to explain

**Figure 21.** Mean and  $1\sigma$  standard deviation of aerosol optical depth (500 nm) and ship-measured extinction ( $\sigma_{\text{sp}} + \sigma_{\text{ap}}$ ) (550 nm, 55  $\pm$  5% RH, sub-10  $\mu\text{m}$ ) for the seven regions.

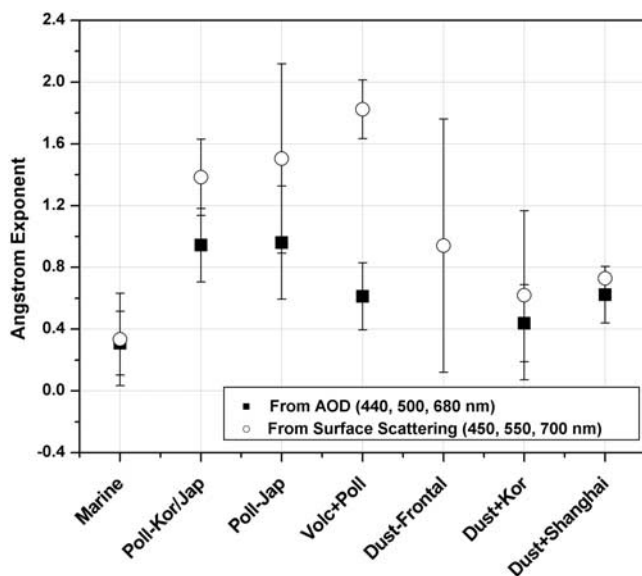


**Figure 22.** Ångström exponent derived from AOD and ship-measured  $\sigma_{sp}$  ( $55 \pm 5\%$  RH, sub- $10\mu\text{m}$ ) at wavelengths near the nephelometer wavelengths of 450, 550, and 700 nm.

the lower column derived  $\text{\AA}$  values relative to the surface derived values.

[101] On DOY 97, a low-pressure center east of Lake Baikal lofted dust to the upper troposphere. In the Polluted – Japan (Figure 23) and Volcano + Polluted (Figure 24) regions, RHB was ahead of the front. Lidar profiles showed distinct aerosol layers aloft during both periods. In addition, the surface seawater temperature was relatively low (7 to  $14^\circ\text{C}$  versus 15 to  $23^\circ\text{C}$  for the other periods in the western Pacific) and there was a strong temperature inversion within a few hundred meters of the surface. As a result there was an aerosol layer near the surface that was isolated from those at higher altitudes. During the Polluted – Japan period, the surface  $\text{\AA}$  was  $36 \pm 32\%$  higher than the column value. On the basis of three sets of lidar measurements, only 13 to 27% of the column extinction was due to aerosol in the lowest layer. During the Volcano + Polluted period, there was a well defined aerosol layer between 4 and 6 km as dust was transported from the dust region out to the Pacific. The combination of a dust layer aloft and the Volcano + Polluted layer near the surface resulted in the highest aerosol optical depths measured on the ship during ACE-Asia. Surface  $\text{\AA}$  was  $66 \pm 77\%$  higher than the column value indicating the presence of relatively larger aerosol in the upper troposphere. Only  $15 \pm 8\%$  of the column extinction was due to the lowest aerosol layer. The Volcano + Polluted region had the lowest concentration of supermicron aerosol surface area. This lack of supermicron aerosol is most likely responsible for the greater difference between the surface and column-derived  $\text{\AA}$  for the Volcano + Polluted period relative to the Polluted – Japan period.

[102] The Dust + Korea and Dust + Shanghai periods occurred after the front had passed RHB on DOY 100.8. After the frontal passage, the pollution and dust aerosol were transported together in the lower troposphere. During the Dust + Korea period, vertical profiles of RH indicated a

well mixed boundary layer with a height varying between 1 and 1.75 km (Figure 24). The aerosol extinction profiles were similar with a well defined aerosol layer within the boundary layer and no significant aerosol extinction above. The surface and column  $\text{\AA}$  agreed within  $29 \pm 96\%$ . On the basis of four sets of lidar measurements, 85 to 94% of the column extinction was due to aerosol in the boundary layer.

[103] During the Dust + Shanghai period, the aerosol extinction was confined to a well-mixed boundary layer that extended to about 700 m (Figure 24). The surface and column derived  $\text{\AA}$  values agreed to within  $15 \pm 64\%$  and  $80 \pm 2.8\%$  of the column extinction was due to aerosol in the boundary layer.

[104] Similar to other regional aerosol experiments studying the outflow of continental aerosol into the marine atmosphere (e.g., Aerosols99 and INDOEX), coupled surface and vertical measurements were essential for identifying conditions during which the surface and upper aerosol were coupled or decoupled.

## 5. Conclusions

[105] Comprehensive measurements of surface aerosol chemical, physical, and optical properties and column optical properties were made on board the R/V *Ronald H. Brown* during ACE-Asia. This data set allowed not only for a characterization of aerosol properties in the ACE-Asia region but also an assessment of how well state-of-the-art measurements and models can characterize such a complex aerosol mixture. The dominant result of ACE-Asia was the impact of dust on the chemical composition, size distribution, and optical properties of the aerosol. Unlike previous regional experiments (ACE 1, Aerosols99, ACE 2, and INDOEX), dust dominated the supermicron and sub- $10\mu\text{m}$  size fractions and made a significant contribution to the submicron size range. As a result, it also dominated the supermicron and sub- $10\mu\text{m}$  light scattering. Interestingly, supermicron single scattering albedos were relatively high ( $0.98 \pm 0.01$  at ambient relative humidity) during dusty periods indicating that the scattering by the dust at mid-visible wavelengths overwhelmed the absorption. Although the aggregation of soot spherules with the supermicron dust did not appear to affect the single scattering albedo, it may have consequences for the radiative impact of the soot by shortening its lifetime in the atmosphere.

[106] A comparison of mass scattering efficiencies for the dominant aerosol chemical components (sea salt, sulfate aerosol, particulate organic material (POM), and dust) from recent regional experiments (ACE 1, Aerosols99, INDOEX, and ACE-Asia) indicates that values are relatively constant and independent of source region. The only exception is supermicron POM. The variability observed between these experiments may be due to differences in the composition and/or size distribution of the organic aerosol or to sampling and analysis procedures.

[107] The approach of an overdetermined data set combined with the complexity of the ACE-Asia aerosol revealed many challenges for the state-of-the-art measurement and modeling techniques employed. Comparisons between measured and calculated aerosol mass and light scattering yielded agreement within overall experimental uncertainty.

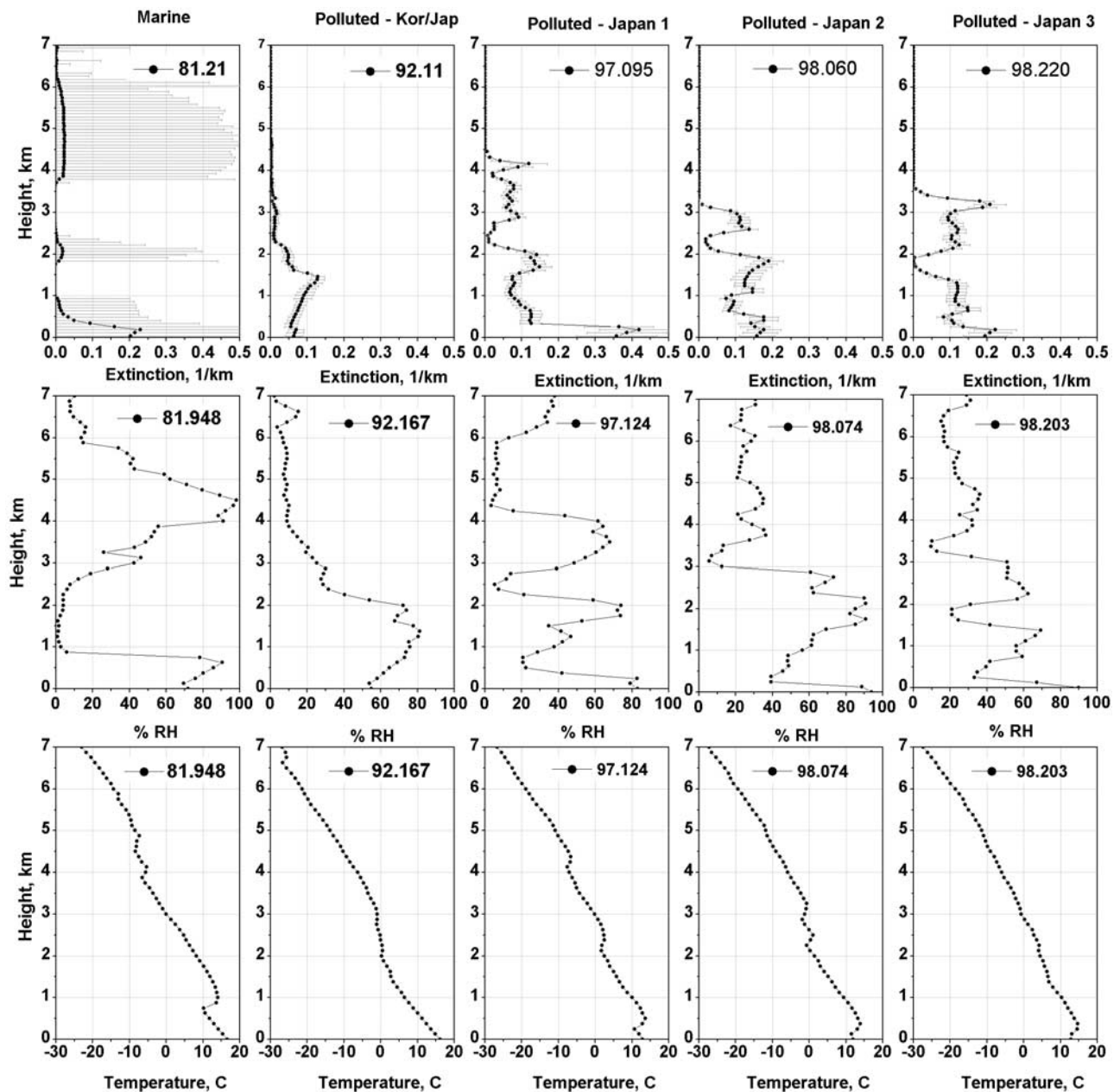


**Figure 23.** (top) Vertical profiles of aerosol extinction from a MPL lidar. Uncertainty is shown by the horizontal lines. (middle) Relative humidity and (bottom) temperature from radiosondes. Data are shown for all available lidar measurements during the Marine, Polluted – Korean/Japan, and Polluted – Japan periods.

This agreement was unsatisfying, however, since it relied on a choice of particle shapes not confirmed by measurements. In addition, it required assumptions about the response of sizing instruments (DMPS and APS) to nonspherical dust particles that have not been verified empirically. A comparison of measured and calculated aerosol absorption coefficients revealed systematic differences for both the submicron and supermicron size ranges that at times were greater than the relatively large overall uncertainty of the methods. As a result, calculated and measured aerosol mass absorption efficiencies showed large discrepancies with

calculated values ranging from 2 to 8  $\text{m}^2 \text{g}^{-1}$  and measured values ranging from 5 to 25  $\text{m}^2 \text{g}^{-1}$ .

[108] Hence a particular challenge presented by the ACE-Asia aerosol is the nonsphericity and mixing state of dust aerosol (how do sizing and optical instruments respond to it and how is it best parameterized in optical models?). Also challenged is the standard of 10  $\text{m}^2 \text{g}^{-1}$  as the mass absorption efficiency of elemental carbon. What does that mean for an aerosol made up of inhomogeneous mixtures of soot and other chemical components in nonspherical particles? These challenges and

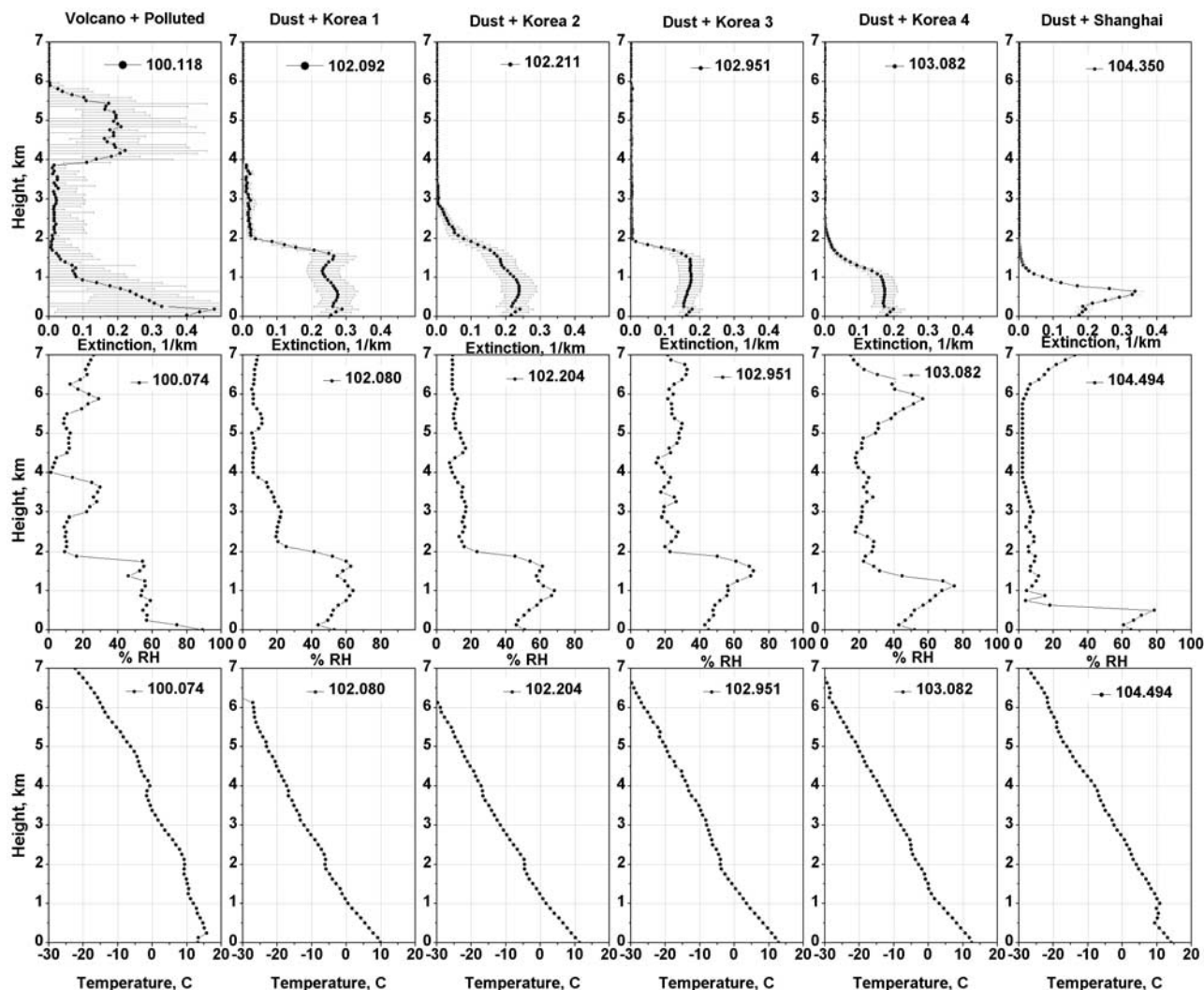


**Figure 24.** Same as Figure 23, but during the Volcano + Polluted, Dust + Korea, and Dust + Shanghai periods.

uncertainties will require further regional intensive experiments that emphasize the collection of overdetermined data sets, instrument characterization, and instrument and model comparisons.

[109] **Acknowledgments.** We thank Drew Hamilton for logistical assistance and the officers and crew of the NOAA research vessel *Ronald H. Brown*. This research was funded by the NOAA OGP's Aerosol and Climate Interactions Program and the National Science Foundation under Grant No. 0086550 (CMC and MJR). Any opinions, findings, and conclusions or recommendations expressed in this paper are those of the authors and do not necessarily reflect the views of the NSF. This is NOAA PMEL contribution number 2587 and JISAO contribution number 993.

## References

- Anderson, T. L., and J. A. Ogren (1998), Determining aerosol radiative properties using the TSI 3563 integrating nephelometer, *Aerosol Sci. Technol.*, *29*, 57–69.
- Anderson, T. L., D. S. Covert, J. D. Wheeler, J. M. Harris, K. D. Perry, B. E. Trost, D. J. Jaffe, and J. A. Ogren (1999), Aerosol backscatter fraction and single scattering albedo: Measured values and uncertainties at a coastal station in the Pacific Northwest, *J. Geophys. Res.*, *104*, 26,793–26,807.
- Anderson, T. L., S. J. Masonis, D. S. Covert, N. C. Ahlquist, S. G. Howell, A. D. Clarke, and C. S. McNaughton (2003), Variability of aerosol optical properties derived from in situ aircraft measurements during ACE-Asia, *J. Geophys. Res.*, *108*(D23), 8647, doi:10.1029/2002JD003247.
- Arimoto, R., T. Kirchner, J. Webb, M. Conley, B. Stewart, and D. Schoep, M. Walthall (2002), 239,240Pu and inorganic substances in aerosols from the vicinity of the waste isolation pilot plant: The importance of resuspension, *Health Phys.*, *83*, 456–470.
- Bates, T. S., D. J. Coffman, D. S. Covert, and P. K. Quinn (2002), Regional marine boundary layer aerosol size distributions in the Indian, Atlantic, and Pacific Oceans: A comparison of INDOEX measurements with ACE-1, ACE-2, and Aerosols99, *J. Geophys. Res.*, *107*(D19), 8026, doi:10.1029/2001JD001174.
- Bates, T. S., et al. (2004), Marine boundary layer dust and pollutant transport associated with the passage of a frontal system over eastern Asia, *J. Geophys. Res.*, *109*, D19S19, doi:10.1029/2003JD004094.
- Bergstrom, R. W. (1972), Predictions of the spectral absorption and extinction coefficients of an urban air pollution model, *Atmos. Environ.*, *6*, 247–258.
- Berner, A., C. Lurzer, F. Pohl, O. Preining, and P. Wagner (1979), The size distribution of the urban aerosol in Vienna, *Sci. Total Environ.*, *13*, 245–261.
- Birch, M. E., and R. A. Cary (1996), Elemental carbon-based method for monitoring occupational exposures to particulate diesel exhaust, *Aerosol Sci. Technol.*, *25*, 221–241.
- Bohren, C. F., and D. R. Huffman (1983), *Absorption and Scattering of Light by Small Particles*, John Wiley, Hoboken, N. J.
- Bond, T. C., T. L. Anderson, and D. Campbell (1999), Calibration and intercomparison of filter-based measurements of visible light absorption by aerosols, *Aerosol Sci. Technol.*, *30*, 582–600.

- Bray, W. H. (1970), Water vapor pressure control with aqueous solutions of sulfuric acid, *J. Mater. JMLSA*, 5, 233–248.
- Cahill, T. A., R. A. Eldred, and P. J. Feeney (1986), Particulate monitoring and data analysis for the National Park Service, 1982–1985, report, Univ. of Calif., Davis.
- Campbell, J. R., D. L. Hlavka, E. J. Welton, C. J. Flynn, D. D. Turner, J. D. Spinhirne, V. S. Scott, and I. H. Hwang (2002), Full-time, eye-safe cloud and aerosol lidar observation at atmospheric radiation measurement program sites: Instrument and data processing, *J. Atmos. Oceanic Technol.*, 19, 431–442.
- Carrico, C. M., P. Kus, M. J. Rood, P. K. Quinn, and T. S. Bates (2003), Mixtures of pollution, dust, sea salt, and volcanic aerosol during ACE-Asia: Aerosol radiative properties as a function of relative humidity, *J. Geophys. Res.*, 108(D23), 8650, doi:10.1029/2003JD003405.
- Charlson, R. J., T. L. Anderson, and H. Rodhe (1999), Direct climate forcing by anthropogenic aerosols: Quantifying the link between atmospheric sulfate and radiation, *Beitr. Phys. Atmos.*, 72(1), 79–94.
- Cheng, Y., B. Chen, and H. Yeh (1990), Behavior of isometric nonspherical aerosol particles in the aerodynamic particle sizer, *J. Aerosol Sci.*, 21, 701–710.
- Cheng, Y., B. Chen, H. Yeh, I. Marshall, J. Mitchell, and W. Griffiths (1993), Behavior of compact nonspherical particles in the TSI aerodynamic particle sizer model APS33B-Ultra-stokesian drag forces, *Aerosol Sci. Technol.*, 19, 255–267.
- Chughtai, A. R., M. E. Brooks, and D. M. Smith (1996), Hydration of black carbon, *J. Geophys. Res.*, 101, 19,505–19,514.
- Clegg, S. L., and P. Brimblecombe (1985), Potential degassing of hydrogen chloride from acidified sodium chloride droplets, *Atmos. Environ.*, 19, 465–470.
- Desboeufs, K. V., R. Losno, and J. L. Colin (2001), Factors influencing aerosol solubility during cloud processes, *Atmos. Environ.*, 35, 3529–3537.
- Deschamps, P.-Y., P. Lecomte, C. Verwaerde, and B. Fougne (2004), SIMBAD: A field radiometer for satellite ocean-color validation, *Appl. Opt.*, in press.
- Draxler, R. R. (1992), Hybrid Single-Particle Lagrangian Integrated Trajectories (HY-SPLIT): version 3. 0, user's guide and model description, *Tech. Rep. ERL ARL-195*, Natl. Oceanic and Atmos. Admin., Silver Spring, Md.
- Feely, R. A., G. J. Massoth, and G. T. Lebon (1991), Sampling of marine particulate matter and analysis by X-ray fluorescence spectrometry, in *Marine Particles: Analysis and Characterization*, *Geophys. Monogr. Ser.*, vol. 63, edited by D. C. Hurd and D. W. Spencer, pp. 251–257, AGU, Washington, D. C.
- Feely, R. A., E. T. Baker, G. T. Lebon, J. F. Gendron, G. J. Massoth, and C. W. Mordy (1998), Chemical variations of hydrothermal particles in the 1996 Gorda Ridge Event and chronic plumes, *Deep Sea Res., Part II*, 45, 2637–2664.
- Fuller, K. A., W. C. Malm, and S. M. Kreidenweis (1999), Effects of mixing on extinction by carbonaceous particles, *J. Geophys. Res.*, 104, 15,941–15,954.
- Heintzenberg, J. (1978), The angular calibration of the total scatter/backscatter nephelometer, consequences and applications, *Staub-Reinhalt Luft*, 38, 62–63.
- Heintzenberg, J., K. Okada, and B. P. Luo (2002), Distribution of optical properties among atmospheric submicrometer particles of given electrical mobilities, *J. Geophys. Res.*, 107(D11), 4107, doi:10.1029/2001JD000372.
- Holland, H. D. (1978), *The Chemistry of the Atmosphere and Oceans*, 154 pp., John Wiley, Hoboken, N. J.
- Huebert, B. J., T. Bates, P. B. Russell, G. Shi, Y. J. Kim, K. Kawamura, G. Carmichael, and T. Nakajima (2003), An overview of ACE-Asia: Strategies for quantifying the relationships between Asian aerosols and their climatic impacts, *J. Geophys. Res.*, 108(D23), 8633, doi:10.1029/2003JD003550.
- Kalashnikova, O. V., and I. N. Sokolik (2002), Importance of shapes and compositions of wind-blown dust particles for remote sensing at solar wavelengths, *Geophys. Res. Lett.*, 29(10), 1398, doi:10.1029/2002GL014947.
- Malm, W. C., J. F. Sisler, D. Huffman, R. A. Eldred, and T. A. Cahill (1994), Spatial and seasonal trends in particle concentration and optical extinction in the United States, *J. Geophys. Res.*, 99, 1347–1370.
- Maria, S. F., L. M. Russell, B. J. Turpin, and R. J. Porcja (2002), FTIR measurements of functional groups and organic mass in aerosol samples over the Caribbean, *Atmos. Environ.*, 36, 5158–5196.
- Maria, S. F., L. M. Russell, B. J. Turpin, R. J. Porcja, T. L. Campos, R. J. Weber, and B. J. Huebert (2003), Source signatures of carbon monoxide and organic functional groups in Asian Pacific Regional Aerosol Characterization Experiment (ACE-Asia) submicron aerosol types, *J. Geophys. Res.*, 108(D23), 8637, doi:10.1029/2003JD003703.
- Martins, J. V., P. Artaxo, C. Lioussé, J. S. Reid, P. V. Hobbs, and Y. J. Kaufman (1998), Effects of black carbon content, particle size, and mixing on light absorption by aerosols from biomass burning in Brazil, *J. Geophys. Res.*, 103, 32,041–32,050.
- Ming, Y., and L. M. Russell (2002), Thermodynamic equilibrium of organic-electrolyte mixtures in aerosol particles, *AIChE J.*, 48, 1331–1348.
- Mishchenko, M. I., L. D. Travis, R. A. Kahn, and R. A. West (1997), Modeling phase functions for dustlike tropospheric aerosols using a shape mixture of randomly oriented polydisperse spheroids, *J. Geophys. Res.*, 102, 16,831–16,847.
- Perry, K. D., T. A. Cahill, R. A. Eldred, D. D. Dutcher, and T. E. Gill (1997), Long-range transport of North African dust to the eastern United States, *J. Geophys. Res.*, 102, 11,225–11,238.
- Porter, J. N., M. A. Miller, C. Motell, and C. Pietras (2001), Use of hand-held Sun photometers for measurements of aerosol optical thickness at sea, *J. Atmos. Oceanic Technol.*, 18, 765–774.
- Prospero, J. M., P. Ginoux, O. Torres, S. E. Nicholson, and T. E. Gill (2002), Environmental characterization of global sources of atmospheric soil dust identified with the Nimbus 7 Total Ozone Mapping Spectrometer (TOMS) absorbing aerosol product, *Rev. Geophys.*, 40(1), 1002, doi:10.1029/2000RG000095.
- Quinn, P. K., and D. J. Coffman (1998), Local closure during the First Aerosol Characterization Experiment (ACE 1): Aerosol mass concentration and scattering and backscattering coefficients, *J. Geophys. Res.*, 103, 16,575–16,596.
- Quinn, P. K., V. N. Kapustin, T. S. Bates, and D. S. Covert (1996), Chemical and optical properties of marine boundary layer aerosol particles of the mid-Pacific in relation to sources and meteorological transport, *J. Geophys. Res.*, 101, 6931–6951.
- Quinn, P. K., D. J. Coffman, V. N. Kapustin, T. S. Bates, and D. S. Covert (1998), Aerosol optical properties in the marine boundary layer during the First Aerosol Characterization Experiment (ACE 1) and the underlying chemical and physical aerosol properties, *J. Geophys. Res.*, 103, 16,547–16,563.
- Quinn, P. K., et al. (2000a), Surface submicron aerosol chemical composition: What fraction is not sulfate?, *J. Geophys. Res.*, 105, 6785–6806.
- Quinn, P. K., T. S. Bates, D. J. Coffman, T. L. Miller, J. E. Johnson, D. S. Covert, J. P. Putaud, C. Neusüss, and T. Novakov (2000b), A comparison of aerosol chemical and optical properties from the first and second aerosol characterization experiments, *Tellus, Ser. B*, 52, 239–257.
- Quinn, P. K., D. J. Coffman, T. S. Bates, T. L. Miller, J. E. Johnson, K. Voss, E. J. Welton, and C. Neusüss (2001), Dominant aerosol chemical components and their contribution to extinction during the Aerosols99 cruise across the Atlantic, *J. Geophys. Res.*, 106, 20,783–20,810.
- Quinn, P. K., D. J. Coffman, T. S. Bates, T. L. Miller, J. E. Johnson, E. J. Welton, C. Neusüss, M. Miller, and P. Sheridan (2002), Aerosol optical properties during INDOEX 1999: Means, variabilities, and controlling factors, *J. Geophys. Res.*, 107(D19), 8020, doi:10.1029/2000JD000037.
- Ramanathan, V., P. J. Crutzen, J. T. Kiehl, and D. Rosenfeld (2001), Aerosols, climate, and the hydrological cycle, *Science*, 294, 2119–2124.
- Reynolds, M. R., M. A. Miller, and M. J. Bartholomew (2001), A fast-rotating, spectral shadowband radiometer for marine applications, *J. Atmos. Oceanic Technol.*, 18, 200–214.
- Savoie, D. L., and J. M. Prospero (1980), Water-soluble potassium, calcium, and magnesium in the aerosols over the tropical North Atlantic, *J. Geophys. Res.*, 85, 385–392.
- Schauer, J. J., et al. (2003), ACE-Asia intercomparison of a thermal-optical method for the determination of particle-phase organic and elemental carbon, *Environ. Sci. Technol.*, 37, 993–1001.
- Seinfeld, J. H. (1986), *Atmospheric Chemistry and Physics of Air Pollution*, 296 pp., John Wiley, Hoboken, N. J.
- Shaw, M. A., and M. J. Rood (1990), Measurement of the crystallization humidities of ambient aerosol particles, *Atmos. Environ., Part A*, 24, 1837–1841.
- Sokolik, I. N., and O. B. Toon (1999), Incorporation of mineralogical composition into models of the radiative properties of mineral aerosol from UV to IR wavelengths, *J. Geophys. Res.*, 104, 9423–9444.
- Spinhirne, J. D., J. Rall, and V. S. Scott (1995), Compact eye-safe lidar systems, *Rev. Laser Eng.*, 23, 26–32.
- Stelson, A. W. (1990), Urban aerosol refractive index prediction by partial molar refraction approach, *Environ. Sci. Technol.*, 24, 1676–1679.
- Tang, I. N., and H. R. Munkelwitz (1991), Simultaneous determination of refractive index and density of an evaporating aqueous solution droplet, *Aerosol Sci. Technol.*, 15, 201–207.
- Tang, I. N., and H. R. Munkelwitz (1994), Water activities, densities, and refractive indices of aqueous sulfates and sodium nitrate droplets of atmospheric importance, *J. Geophys. Res.*, 99, 18,801–18,808.

- Tang, I. N., A. C. Tridico, and K. H. Fung (1997), Thermodynamic and optical properties of sea salt aerosols, *J. Geophys. Res.*, *102*, 23,269–23,275.
- Turpin, B. J., and H. Lim (2001), Species contribution to PM<sub>2.5</sub> concentrations: Revisiting common assumptions for estimating organic mass, *Aerosol Sci. Technol.*, *35*, 602–610.
- Turpin, B. J., J. J. Huntzicker, and S. V. Hering (1994), Investigation of organic aerosol sampling artifacts in the Los Angeles Base, *Atmos. Environ.*, *28*, 23,061–23,071.
- Turpin, B. J., P. Saxena, and E. Andrews (2000), Measuring and simulating particulate organics in the atmosphere: Problems and prospects, *Atmos. Environ.*, *34*, 2983–3013.
- Wang, H., and W. John (1987), Particle density correction for the aerodynamic particle sizer, *Aerosol Sci. Technol.*, *6*, 191–198.
- Welton, E. J., and J. R. Campbell (2002), Micro-pulse lidar signals: Uncertainty analysis, *J. Atmos. Oceanic Technol.*, *19*, 2089–2094.
- Welton, E. J., et al. (2000), Ground-based Lidar measurements of aerosols during ACE-2: Instrument description, results, and comparisons with other ground-based and airborne measurements, *Tellus, Ser. B*, *52*, 635–650.
- Welton, E. J., K. J. Voss, P. K. Quinn, P. J. Flatau, K. Markowicz, J. R. Campbell, J. D. Spinhirne, H. R. Gordon, and J. E. Johnson (2002), Measurements of aerosol vertical profiles and optical properties during INDOEX 1999 using micropulse lidars, *J. Geophys. Res.*, *107*(D19), 8019, doi:10.1029/2000JD000038.
- 
- J. Anderson, Department of Mechanical and Aerospace Engineering, Arizona State University, University Boulevard, Tempe, AZ 85287, USA.
- R. Arimoto, Carlsbad Environmental Monitoring and Research Center, New Mexico State University, 1400 University Drive, Carlsbad, NM 88220, USA.
- T. S. Bates, D. J. Coffman, J. E. Johnson, T. L. Miller, and P. K. Quinn, Pacific Marine Environmental Laboratory, National Oceanic and Atmospheric Administration, 7600 San Point Way, NE, Seattle, WA 98115, USA. (patricia.k.quinn@noaa.gov)
- C. M. Carrico and M. J. Rood, Department of Civil and Environmental Engineering, University of Illinois, 205 North Mathews Avenue, Urbana, IL 61801, USA.
- D. S. Covert, Joint Institute for the Study of the Atmosphere and Ocean, University of Washington, Seattle, WA 98195, USA.
- S. Maria and L. Russell, Department of Chemical Engineering, Princeton University, A317 Engineering Quadrangle, Princeton, NJ 08544, USA.
- E. J. Welton, Goddard Space Flight Center, NASA, Greenbelt, MD 20771, USA.